DESY 11-248 ISSN 0418-9833
December 2011

Measurement of Inclusive and Dijet D^* Meson Cross Sections in Photoproduction at HERA

H1 Collaboration

Abstract

The inclusive photoproduction of D^* mesons and of D^*-tagged dijets is investigated with the H1 detector at the ep collider HERA. The kinematic region covers small photon virtualities $Q^2 < 2\ \mathrm{GeV}^2$ and photon-proton centre-of-mass energies of $100 < W_{\gamma p} < 285\ \mathrm{GeV}$. Inclusive D^* meson differential cross sections are measured for central rapidities $|\eta(D^*)| < 1.5$ and transverse momenta $p_T(D^*) > 1.8\ \mathrm{GeV}$. The heavy quark production process is further investigated in events with at least two jets with transverse momentum $p_T(\mathrm{jet}) > 3.5\ \mathrm{GeV}$ each, one containing the D^* meson. Differential cross sections for D^*-tagged dijet production and for correlations between the jets are measured in the range $|\eta(D^*)| < 1.5$ and $p_T(D^*) > 2.1\ \mathrm{GeV}$. The results are compared with predictions from Monte Carlo simulations and next-to-leading order perturbative QCD calculations.

Submitted to Eur. Phys. J. **C**

F.D. Aaron[5,48], C. Alexa[5], V. Andreev[25], S. Backovic[30], A. Baghdasaryan[38], S. Baghdasaryan[38], E. Barrelet[29], W. Bartel[11], K. Begzsuren[35], A. Belousov[25], P. Belov[11], J.C. Bizot[27], M.-O. Boenig[8], V. Boudry[28], I. Bozovic-Jelisavcic[2], J. Bracinik[3], G. Brandt[11], M. Brinkmann[11], V. Brisson[27], D. Britzger[11], D. Bruncko[16], A. Bunyatyan[13,38], G. Buschhorn[26,†], L. Bystritskaya[24], A.J. Campbell[11], K.B. Cantun Avila[22], F. Ceccopieri[4], K. Cerny[32], V. Cerny[16,47], V. Chekelian[26], J.G. Contreras[22], J.A. Coughlan[6], J. Cvach[31], J.B. Dainton[18], K. Daum[37,43], B. Delcourt[27], J. Delvax[4], E.A. De Wolf[4], C. Diaconu[21], M. Dobre[12,50,51], V. Dodonov[13], A. Dossanov[26], A. Dubak[30,46], G. Eckerlin[11], S. Egli[36], A. Eliseev[25], E. Elsen[11], L. Favart[4], A. Fedotov[24], R. Felst[11], J. Feltesse[10], J. Ferencei[16], D.-J. Fischer[11], M. Fleischer[11], A. Fomenko[25], E. Gabathuler[18], J. Gayler[11], S. Ghazaryan[11], A. Glazov[11], L. Goerlich[7], N. Gogitidze[25], M. Gouzevitch[11,45], C. Grab[40], A. Grebenyuk[11], T. Greenshaw[18], G. Grindhammer[26], S. Habib[11], D. Haidt[11], C. Helebrant[11], R.C.W. Henderson[17], E. Hennekemper[15], H. Henschel[39], M. Herbst[15], G. Herrera[23], M. Hildebrandt[36], K.H. Hiller[39], D. Hoffmann[21], R. Horisberger[36], T. Hreus[4,44], F. Huber[14], M. Jacquet[27], X. Janssen[4], L. Jönsson[20], A.W. Jung[15], H. Jung[11,4,52], M. Kapichine[9], I.R. Kenyon[3], C. Kiesling[26], M. Klein[18], C. Kleinwort[11], T. Kluge[18], R. Kogler[11], P. Kostka[39], M. Krämer[11], J. Kretzschmar[18], K. Krüger[15], M.P.J. Landon[19], W. Lange[39], G. Laštovička-Medin[30], P. Laycock[18], A. Lebedev[25], V. Lendermann[15], S. Levonian[11], K. Lipka[11,50], B. List[11], J. List[11], R. Lopez-Fernandez[23], V. Lubimov[24], A. Makankine[9], E. Malinovski[25], H.-U. Martyn[1], S.J. Maxfield[18], A. Mehta[18], A.B. Meyer[11], H. Meyer[37], J. Meyer[11], S. Mikocki[7], I. Milcewicz-Mika[7], F. Moreau[28], A. Morozov[9], J.V. Morris[6], M. Mudrinic[2], K. Müller[41], Th. Naumann[39], P.R. Newman[3], C. Niebuhr[11], D. Nikitin[9], G. Nowak[7], K. Nowak[11], J.E. Olsson[11], D. Ozerov[24], P. Pahl[11], V. Palichik[9], I. Panagoulias[l,11,42], M. Pandurovic[2], Th. Papadopoulou[l,11,42], C. Pascaud[27], G.D. Patel[18], E. Perez[10,45], A. Petrukhin[11], I. Picuric[30], S. Piec[11], H. Pirumov[14], D. Pitzl[11], R. Plačakytė[11], B. Pokorny[32], R. Polifka[32,53], B. Povh[13], V. Radescu[11], N. Raicevic[30], T. Ravdandorj[35], P. Reimer[31], E. Rizvi[19], P. Robmann[41], R. Roosen[4], A. Rostovtsev[24], M. Rotaru[5], J.E. Ruiz Tabasco[22], S. Rusakov[25], D. Šálek[32], D.P.C. Sankey[6], M. Sauter[14], E. Sauvan[21], S. Schmitt[11], L. Schoeffel[10], A. Schöning[14], H.-C. Schultz-Coulon[15], F. Sefkow[11], L.N. Shtarkov[25], S. Shushkevich[11], T. Sloan[17], I. Smiljanic[2], Y. Soloviev[25], P. Sopicki[7], D. South[11], V. Spaskov[9], A. Specka[28], Z. Staykova[4], M. Steder[11], B. Stella[33], G. Stoicea[5], U. Straumann[41], T. Sykora[4,32], P.D. Thompson[3], T.H. Tran[27], D. Traynor[19], P. Truöl[41], I. Tsakov[34], B. Tseepeldorj[35,49], J. Turnau[7], K. Urban[15], A. Valkárová[32], C. Vallée[21], P. Van Mechelen[4], Y. Vazdik[25], D. Wegener[8], E. Wünsch[11], J. Žáček[32], J. Zálešák[31], Z. Zhang[27], A. Zhokin[24], H. Zohrabyan[38], and F. Zomer[27]

[1] *I. Physikalisches Institut der RWTH, Aachen, Germany*
[2] *Vinca Institute of Nuclear Sciences, University of Belgrade, 1100 Belgrade, Serbia*
[3] *School of Physics and Astronomy, University of Birmingham, Birmingham, UK*[b]
[4] *Inter-University Institute for High Energies ULB-VUB, Brussels and Universiteit Antwerpen, Antwerpen, Belgium*[c]
[5] *National Institute for Physics and Nuclear Engineering (NIPNE) , Bucharest, Romania*[m]
[6] *Rutherford Appleton Laboratory, Chilton, Didcot, UK*[b]
[7] *Institute for Nuclear Physics, Cracow, Poland*[d]
[8] *Institut für Physik, TU Dortmund, Dortmund, Germany*[a]
[9] *Joint Institute for Nuclear Research, Dubna, Russia*

[10] *CEA, DSM/Irfu, CE-Saclay, Gif-sur-Yvette, France*
[11] *DESY, Hamburg, Germany*
[12] *Institut für Experimentalphysik, Universität Hamburg, Hamburg, Germany*[a]
[13] *Max-Planck-Institut für Kernphysik, Heidelberg, Germany*
[14] *Physikalisches Institut, Universität Heidelberg, Heidelberg, Germany*[a]
[15] *Kirchhoff-Institut für Physik, Universität Heidelberg, Heidelberg, Germany*[a]
[16] *Institute of Experimental Physics, Slovak Academy of Sciences, Košice, Slovak Republic*[f]
[17] *Department of Physics, University of Lancaster, Lancaster, UK*[b]
[18] *Department of Physics, University of Liverpool, Liverpool, UK*[b]
[19] *School of Physics and Astronomy, Queen Mary, University of London, London, UK*[b]
[20] *Physics Department, University of Lund, Lund, Sweden*[g]
[21] *CPPM, Aix-Marseille Univ, CNRS/IN2P3, 13288 Marseille, France*
[22] *Departamento de Fisica Aplicada, CINVESTAV, Mérida, Yucatán, México*[j]
[23] *Departamento de Fisica, CINVESTAV IPN, México City, México*[j]
[24] *Institute for Theoretical and Experimental Physics, Moscow, Russia*[k]
[25] *Lebedev Physical Institute, Moscow, Russia*[e]
[26] *Max-Planck-Institut für Physik, München, Germany*
[27] *LAL, Université Paris-Sud, CNRS/IN2P3, Orsay, France*
[28] *LLR, Ecole Polytechnique, CNRS/IN2P3, Palaiseau, France*
[29] *LPNHE, Université Pierre et Marie Curie Paris 6, Université Denis Diderot Paris 7, CNRS/IN2P3, Paris, France*
[30] *Faculty of Science, University of Montenegro, Podgorica, Montenegro*[n]
[31] *Institute of Physics, Academy of Sciences of the Czech Republic, Praha, Czech Republic*[h]
[32] *Faculty of Mathematics and Physics, Charles University, Praha, Czech Republic*[h]
[33] *Dipartimento di Fisica Università di Roma Tre and INFN Roma 3, Roma, Italy*
[34] *Institute for Nuclear Research and Nuclear Energy, Sofia, Bulgaria*[e]
[35] *Institute of Physics and Technology of the Mongolian Academy of Sciences, Ulaanbaatar, Mongolia*
[36] *Paul Scherrer Institut, Villigen, Switzerland*
[37] *Fachbereich C, Universität Wuppertal, Wuppertal, Germany*
[38] *Yerevan Physics Institute, Yerevan, Armenia*
[39] *DESY, Zeuthen, Germany*
[40] *Institut für Teilchenphysik, ETH, Zürich, Switzerland*[i]
[41] *Physik-Institut der Universität Zürich, Zürich, Switzerland*[i]

[42] *Also at Physics Department, National Technical University, Zografou Campus, GR-15773 Athens, Greece*
[43] *Also at Rechenzentrum, Universität Wuppertal, Wuppertal, Germany*
[44] *Also at University of P.J. Šafárik, Košice, Slovak Republic*
[45] *Also at CERN, Geneva, Switzerland*
[46] *Also at Max-Planck-Institut für Physik, München, Germany*
[47] *Also at Comenius University, Bratislava, Slovak Republic*
[48] *Also at Faculty of Physics, University of Bucharest, Bucharest, Romania*
[49] *Also at Ulaanbaatar University, Ulaanbaatar, Mongolia*
[50] *Supported by the Initiative and Networking Fund of the Helmholtz Association (HGF) under the contract VH-NG-401.*

[51] *Absent on leave from NIPNE-HH, Bucharest, Romania*
[52] *On leave of absence at CERN, Geneva, Switzerland*
[53] *Also at Department of Physics, University of Toronto, Toronto, Ontario, Canada M5S 1A7*
[†] *Deceased*

[a] *Supported by the Bundesministerium für Bildung und Forschung, FRG, under contract numbers 05H09GUF, 05H09VHC, 05H09VHF, 05H16PEA*
[b] *Supported by the UK Science and Technology Facilities Council, and formerly by the UK Particle Physics and Astronomy Research Council*
[c] *Supported by FNRS-FWO-Vlaanderen, IISN-IIKW and IWT and by Interuniversity Attraction Poles Programme, Belgian Science Policy*
[d] *Partially Supported by Polish Ministry of Science and Higher Education, grant DPN/N168/DESY/2009*
[e] *Supported by the Deutsche Forschungsgemeinschaft*
[f] *Supported by VEGA SR grant no. 2/7062/ 27*
[g] *Supported by the Swedish Natural Science Research Council*
[h] *Supported by the Ministry of Education of the Czech Republic under the projects LC527, INGO-LA09042 and MSM0021620859*
[i] *Supported by the Swiss National Science Foundation*
[j] *Supported by CONACYT, México, grant 48778-F*
[k] *Russian Foundation for Basic Research (RFBR), grant no 1329.2008.2 and Rosatom*
[l] *This project is co-funded by the European Social Fund (75%) and National Resources (25%) - (EPEAEK II) - PYTHAGORAS II*
[m] *Supported by the Romanian National Authority for Scientific Research under the contract PN 09370101*
[n] *Partially Supported by Ministry of Science of Montenegro, no. 05-1/3-3352*

1 Introduction

At the electron-proton collider HERA charm quarks are predominantly produced via boson gluon fusion, $\gamma g \to c\bar{c}$, where the photon is emitted from the incoming lepton and the gluon originates from the proton. The cross section is largest for photoproduction, i.e. for photons with negative four-momentum squared (virtuality) $Q^2 \simeq 0\ \mathrm{GeV}^2$. In addition to hard direct scattering off the photon, processes have to be considered in which the partonic structure of the photon is resolved. The charm quark mass provides a hard scale which justifies the applicability of perturbative QCD (pQCD).

Previous measurements of the photoproduction of charm quarks at HERA cover inclusive D^* meson production [1–3], production of D^* mesons with associated dijets [1,3–5] and heavy quark production using events with a D^* meson and a muon [6]. In this paper, single and double differential cross sections are presented for the inclusive production of D^* mesons and the production of two jets with one of the jets containing the D^* meson. They are compared to leading and next-to-leading order pQCD predictions using different hadronisation models. Compared to the previous H1 analysis of inclusive D^* photoproduction [3], a seven times larger signal sample is analysed here.

Studying events in which at least two jets could be reconstructed, with one of the jets containing the D^* meson, allows further investigations of the details of the heavy quark production process. The jets are measured down to transverse momenta of $p_T(\text{jet}) = 3.5\ \mathrm{GeV}$. While the jet containing the D^* meson originates from a charm or anticharm quark produced in the hard subprocess, the non-D^*-tagged jet, refered to as *other jet*, can result from either the other heavy quark or a light parton (e.g. a gluon). Correlations between the two jets are studied using variables which are sensitive to higher order effects and to the longitudinal as well as to the transverse momentum components of the partons entering the hard scattering process.

2 QCD Calculations

The data presented in this analysis are compared with Monte Carlo simulations based on leading order (LO) matrix elements supplemented by parton showers and with next-to-leading order (NLO) calculations. The calculations are performed using either the collinear factorisation or the k_t-factorisation approach. The collinear factorisation makes use of the DGLAP [7] evolution equations, while in k_t-factorisation the CCFM [8] evolution equations are employed. In the collinear approach transverse momenta obtained through the initial state QCD evolution are neglected and the transverse momenta are generated in the hard scattering process. Effects from the non-vanishing transverse momenta of the gluons enter only at the NLO level. In the k_t-factorisation ansatz the transverse momenta of incoming gluons, k_t, are already included at leading order both in the off-shell matrix element and the k_t-dependent unintegrated gluon density [9]. Corrections appearing only at higher order in collinear factorisation are hence partially included at LO in the k_t-factorisation approach.

For charm quark photoproduction two classes of processes occur, the direct-photon and the resolved-photon processes. In the direct processes the photon emitted from the beam lepton enters directly the hard interaction, whereas in the resolved processes the photon acts as the source of incoming partons, one of which takes part in the hard interaction. The distinction between these two classes depends on the factorisation scheme and the order in which the calculation is performed.

The production of heavy quarks is calculated either in the massive scheme, where heavy quarks are produced only perturbatively via boson gluon fusion, or in the massless scheme, where heavy quarks are treated as massless partons. These two schemes are expected to be appropriate in different regions of phase space [10]: the massive scheme is expected to be reliable when the transverse momentum p_T of the heavy quark is of similar size compared to the charm mass m_c, whereas the massless scheme is expected to be valid for $p_T \gg m_c$. In the general-mass variable-flavour-number scheme (GMVFNS) a smooth transition from the massive to the massless scheme is provided. The structure of the proton and of the photon are described by parton distribution functions (PDFs), that have been determined by fits to data in various heavy flavour schemes and at different orders of pQCD.

Monte Carlo (MC) generators are used to simulate detector effects in order to determine the acceptance and the efficiency for selecting events and to estimate the systematic uncertainties associated with the measurement. The generated events are passed through a detailed simulation of the detector response based on the GEANT simulation programm [11] and are processed using the same reconstruction and analysis chain as is used for the data. The following two MC generators are used:

PYTHIA: The MC program PYTHIA [12] is based on LO QCD matrix elements with leading-log parton showers in the collinear factorisation approach. PYTHIA includes both direct photon gluon fusion and resolved-photon processes. In the resolved-photon processes either a charm quark or a gluon from the photon enters the hard scattering. In the inclusive mode of PYTHIA used here charm quarks are treated as massless partons in all steps of the calculation in both types of processes. The hadronisation process is simulated using the Lund string fragmentation model [13]. The Bowler fragmentation model [14] is applied to fragment the charm quark into a D^* meson. The longitudinal part of the fragmentation is reweighted to the parameterisation by Kartvelishvili et al. [15] which depends on a single parameter α. The latter is set to the values determined by H1 [16], which depend on the centre-of-mass energy squared of the hard subprocess $\hat{s}$ (see table 1). The proton structure is described by the PDF set CTEQ6L [17]. For the photon the PDF set GRV-G LO [18] is used.

CASCADE: The CASCADE [19] MC program is used for simulating events based on LO QCD calculations in the k_t-factorisation approach. The direct boson gluon fusion process is implemented using off-shell matrix elements and incoming gluons which can have non-vanishing transverse momenta. Higher order QCD corrections are simulated with initial state parton showers applying the CCFM evolution [8]. The unintegrated PDFs of the proton from set A0 [20] are used. The hadronisation of partons is performed with the Lund string model as implemented in PYTHIA. For the fragmentation of the charm quarks into D^* mesons the same reweighting procedure to the parameterisation of Kartvelishvili et al. is applied as in the case of PYTHIA.

Fragmentation parameter α					
		PYTHIA		**CASCADE**	
	$\hat{s}_{threshold}$ [GeV^2]	α for $\hat{s} < \hat{s}_{threshold}$	α for $\hat{s} \geq \hat{s}_{threshold}$	α for $\hat{s} < \hat{s}_{threshold}$	α for $\hat{s} \geq \hat{s}_{threshold}$
Central value	70	10.3	4.4	8.4	4.5
Variations	70	8.7	3.9	7.3	3.9
	70	12.2	5.0	9.8	5.1
	50	10.3	4.4	8.4	4.5
	90	10.3	4.4	8.4	4.5

Table 1: Fragmentation parameters α in the Kartvelishvili parameterisation used in the MC simulations. In the two regions of the invariant mass squared of the $c\bar{c}$ pair, $\hat{s}$, separated by the boundary $\hat{s}_{threshold}$, two different values of α are used.

For the comparison of data with NLO predictions, calculations based on the massive approach and the general mass variable flavor number scheme are used. The uncertainties of the calculations are estimated by varying the charm mass, m_c, the factorisation scale, μ_f, and the renormalisation scale, μ_r. The detailed settings are given in table 2. For the comparison in the D^*-tagged dijet sample only MC@NLO is used since it provides a full hadronisation of the final state.

	FMNR			**GMVFNS**			**MC@NLO**		
Parameter	Central	Variations		Central	Variations		Central	Variations	
Charm mass m_c/GeV	1.5	1.3	1.7	1.5			1.5	1.3	1.7
Renorm. Scale μ_r/m_T	1	0.5	2	1	0.5	2	1	0.5	2
Fact. Scale μ_f/m_T	2	1	4	1	0.5	2	2	1	4

Table 2: Parameters and variations used in the NLO calculations of FMNR [21, 22], GMVFNS [26, 27] and MC@NLO [31].

FMNR: The FMNR program [21, 22] is based on an NLO calculation in the massive scheme in the collinear approach. The resolved and direct processes are calculated separately. The program provides weighted parton level events with two or three outgoing partons, i.e. a charm quark pair and possibly one additional light parton. The fragmentation of a charm quark to a D^* meson is treated by a downscaling of the three-momentum of the quark in the charm-anticharm rest frame according to the Peterson fragmentation function with a parameter value of $\epsilon = 0.035$. The PDF sets HERAPDF1.0[1] [23] for the proton

[1] The HERAPDF1.0 set was determined from inclusive deep-inelastic scattering data from the H1 and ZEUS experiments in the GMVFNS. It has been checked that the difference to a PDF set determined in the massive scheme, CTEQ5F3 [24], is significantly smaller than the effect of the variations considered for the systematic uncertainty of the FMNR predictions.

and GRV-G HO [18] for the photon are used. For the strong coupling, the five-flavour QCD scale $\Lambda^{(5)}_{QCD}$ is set to 0.2626 GeV. The charm mass is set to $m_c = 1.5$ GeV and varied by ± 0.2 GeV for an uncertainty estimate. This variation covers the central value for the pole mass of the charm quark [25]. The renormalisation and factorisation scale are set to $\mu_r = m_T$ and $\mu_f = 2 \cdot m_T$ with m_T being the transverse massdefined as $m_T^2 = m_c^2 + (p_{T,c}^2 + p_{T,\bar{c}}^2)/2$, with $p_{T,c}$ and $p_{T,\bar{c}}$ denoting the transverse momenta of the charm and anticharm quark, respectively. In order to estimate the uncertainties related to missing higher orders, the renormalisation and factorisation scales are varied by a factor 2 up and down. Each variation is done independently, leading to in total 6 variations. The resulting uncertainties are added in quadrature separately for positive and negative deviations to obtain the total uncertainties.

GMVFNS: A next to leading order cross section prediction for direct and resolved contributions to the cross section has been provided in the GMVFNS [26,27]. The transition from the charm quark to the D^* meson is given by the KKKS fragmentation function which takes DGLAP evolution and finite-mass effects into account [28]. The parton contents of the proton and of the photon are described by the PDF sets HERAPDF1.0 [23] and AFG04 [29], respectively. The charm mass is set to $m_c = 1.5$ GeV, and the renormalisation and factorisation scales are chosen to be $\mu_r = \mu_f = m_T$. The uncertainties related to missing higher orders are estimated by varying the renormalisation scale, the factorisation scale for the initial state and the factorisation scale for the final state independently by a factor 2 up and down while satisfying the condition that the ratio of any of the two scales is $1/2$, 1 or 2. This leads to 14 independent variations. The maximum and minimum values found by this procedure are used to determine the systematic uncertainty [27].

MC@NLO: In the MC@NLO framework [30], predictions for heavy flavour production at HERA [31] are provided which combine an NLO calculation in the massive approach with parton showers and hadronisation. The direct and resolved part of the cross section are calculated separately. MC@NLO uses parton showers with angular ordering to simulate higher order contributions and the cluster fragmentation as implemented in HERWIG [32]. A factor of 1.34 is applied to the MC@NLO predictions in order to correct the $c \to D^*$ branching fraction in HERWIG to the experimental value [33]. The PDF sets HERAPDF1.0 [23] for the proton and GRV-G HO [18] for the photon are used. For an estimation of the uncertainty, the charm mass and the renomalisation and factorisation scales are varied separately, and the resulting uncertainties are added in quadrature.

3 H1 Detector

A detailed description of the H1 detector can be found elsewhere [34]. Only the components essential to the present analysis are described here.

The origin of the H1 coordinate system is the nominal ep interaction point. The positive z-axis (forward direction) is defined by the direction of the proton beam. Transverse momenta are measured in the x–y plane. Polar (θ) and azimuthal (φ) angles are measured with respect to this reference system. The pseudorapidity is defined as $\eta = -\ln\tan(\theta/2)$.

Charged particles are measured within the central tracking detector (CTD) in the pseudorapidity range $-1.74 < \eta < 1.74$. The CTD comprises two large cylindrical jet chambers (inner CJC1 and outer CJC2) and the silicon vertex detector [35]. The CJCs are separated by a drift chamber which improves the z coordinate reconstruction. A multiwire proportional chamber mainly used for triggering [36] is situated inside the CJC1. These detectors are arranged concentrically around the interaction region in a solenoidal magnetic field of 1.16 T. The trajectories of the charged particles are measured with a transverse momentum resolution of $\sigma(p_T)/p_T \approx 0.5\%\, p_T/\mathrm{GeV} \oplus 1.5\%$ [37]. The CJCs also provide a measurement of the specific ionisation energy loss $\mathrm{d}E/\mathrm{d}x$ of charged particles. The interaction vertex is reconstructed from CTD tracks. The CTD also provides trigger information based on track segments measured in the CJCs [38]. At the first two levels of this fast track trigger (FTT) tracks are reconstructed online from the track segments in the CJCs. At the third level of the FTT invariant masses of combinations of tracks are calculated [39, 40].

Charged and neutral particles are measured with the liquid argon (LAr) calorimeter, which surrounds the tracking chambers. It covers the range $-1.5 < \eta < 3.4$ with full azimuthal acceptance. Electromagnetic shower energies are measured with a precision of $\sigma(E)/E = 12\%/\sqrt{E/\mathrm{GeV}} \oplus 1\%$ and hadronic energies with $\sigma(E)/E = 50\%/\sqrt{E/\mathrm{GeV}} \oplus 2\%$, as determined in test beam measurements [41]. A lead-scintillating fibre calorimeter (SpaCal) [42] covering the backward region $-4.0 < \eta < -1.4$ completes the measurement of charged and neutral particles. For electrons a relative energy resolution of $\sigma(E)/E = 7\%/\sqrt{E/\mathrm{GeV}} \oplus 1\%$ is reached, as determined in test beam measurements [43]. The hadronic final state is reconstructed using an energy flow algorithm which combines charged particles measured in the CTD with information from the SpaCal and LAr calorimeters [44].

The luminosity determination is based on the measurement of the Bethe-Heitler process $ep \to ep\gamma$ where the photon is detected in a calorimeter located at $z = -104$ m downstream of the interaction region in the electron beam direction.

4 Event Selection and Reconstruction

The data sample was recorded in the years 2006 and 2007, when electrons with an energy of 27.6 GeV were collided with protons with 920 GeV.

Photoproduction events are selected by requiring that no isolated high energy electromagnetic cluster, consistent with a signal from a scattered electron, is detected in the calorimeters. This limits the photon virtuality to $Q^2 < 2\ \mathrm{GeV}^2$.

4.1 Inclusive D^* Sample

The triggering of the events relies on the reconstruction of the final state particles originating from the D^* decay. For this purpose all three levels of the FTT are used. At the first level, where tracks are reconstructed only in the transverse plane, the selection criteria are based on track multiplicities above certain transverse momentum thresholds. These conditions are refined on the second level, and on the third level invariant masses and charge combinations consistent with the decay channel $D^{*\pm} \to D^0\pi^{\pm}_{slow} \to K^{\mp}\pi^{\pm}\pi^{\pm}_{slow}$ are required [40]. Three trigger conditions with different thresholds for the transverse momentum of the D^* candidate are used. The analysis is therefore performed in three separate $p_T(D^*)$ regions corresponding to the different luminosities: $\mathcal{L} = 30.7\ \mathrm{pb}^{-1}$ for $1.8 \leq p_T(D^*) < 2.5\ \mathrm{GeV}$, $\mathcal{L} = 68.2\ \mathrm{pb}^{-1}$ for $2.5 \leq p_T(D^*) < 4.5\ \mathrm{GeV}$, and $\mathcal{L} = 93.4\ \mathrm{pb}^{-1}$ for $p_T(D^*) \geq 4.5\ \mathrm{GeV}$. The requirement that all decay particles have to be in the acceptance of the CJC limits the analysis to central rapidities for the D^* meson $|\eta(D^*)| < 1.5$ and photon-proton centre-of-mass energies in the range $100 < W_{\gamma p} < 285\ \mathrm{GeV}$.

The γp centre-of-mass energy is reconstructed using the Jacquet-Blondel method [45]: $W_{\gamma p} = \sqrt{y_{JB}\, s}$ with $y_{JB} = \sum_{HFS}(E - p_z)_i/(2\ E_e)$, where s and E_e denote the square of the ep centre-of-mass energy and the energy of the incoming electron, respectively, and the sum $\sum_{HFS}$ runs over the energy E and the longitudinal momentum p_z of all final state particles. The D^* inelasticity $z(D^*)$, which corresponds to the fraction of photon energy transferred to the D^* meson in the proton rest frame, is defined by $z(D^*) = P \cdot p(D^*)/(P \cdot q)$, with P, $p(D^*)$ and q denoting the four-momenta of the incoming proton, the D^* meson and the exchanged photon, respectively. It is reconstructed as $z(D^*) = (E - p_z)_{D^*}/(2\ y_{JB}\ E_e)$. The inelasticity distribution is sensitive to the kinematics of the production mechanism and to the $c \to D^*$ fragmentation function.

The D^* meson is detected via the decay channel $D^{*\pm} \to D^0\pi^{\pm}_{slow} \to K^{\mp}\pi^{\pm}\pi^{\pm}_{slow}$ with a branching fraction of $\mathcal{BR} = 2.63 \pm 0.04\%$ [25]. The tracks of the decay particles are reconstructed using the CTD information. The invariant mass of the $K^{\mp}\pi^{\pm}$ system is required to be consistent with the nominal D^0 mass [25] within $\pm 80\ \mathrm{MeV}$. The signal to background ratio is improved by applying a loose particle identification criterion to the kaon candidates based on the measurement of the specific energy loss, $\mathrm{d}E/\mathrm{d}x$, in the CTD. In addition the background is reduced by a cut on the fraction of the transverse momentum carried by the D^* with respect to the scalar sum of transverse energies of the hadronic final state, excluding the forward region ($\theta < 10°$). This fraction is required to be $p_T(D^*)/(\sum_{HFS}^{\theta > 10°} E_{T,i}) > 0.1$. This criterion accounts for the harder fragmentation of charm compared to light flavours.

The $D^{*\pm}$ candidates are selected using the mass difference method [46]. In figure 1a) the distribution of the mass difference $\Delta M = m(K\pi\pi_{slow}) - m(K\pi)$ of the final D^* candidates is shown. A clear peak is observed around the nominal value of $\Delta M = 145.4\ \mathrm{MeV}$ [25].

The wrong charge combinations, defined as $K^{\pm}\pi^{\pm}\pi^{\mp}_{slow}$ with $K^{\pm}\pi^{\pm}$ pairs in the accepted D^0 mass range, are used to constrain the shape of the combinatorial background in the signal region. The number of reconstructed D^* mesons $N(D^*)$ is extracted in each analysis bin by a log-likelihood fit simultaneously to the right charge and the wrong charge ΔM distribution. For the signal which has a tail towards larger ΔM values the asymmetric Crystal Ball function [47] is used. The shape of the background is parametrised with the Granet function [48]. The fit is performed in the RooFit framework [49]. The fit to the inclusive data sample yields 8232 ± 164 D^* mesons. To improve the convergence of the fit in each analysis bin, the parameters describing the asymmetry of the Crystal Ball function are fixed to the values found by the fit to the complete data set. The width of the peak varies in dependence on the D^* kinematics and is therefore left free. More details can be found in [50].

4.2 D^*-tagged dijet Sample

For the selection of the D^* meson in the D^*-tagged dijet sample, the requirements are the same as for the inclusive D^* sample, except that the requirement on the specific energy loss $\mathrm{d}E/\mathrm{d}x$ is removed, and the cut on $p_T(D^*)$ is increased to 2.1 GeV because of large backgrounds at small transverse momenta.

Jets are defined by the inclusive k_t-algorithm [51] in the energy recombination scheme with jet size $\Delta R = \sqrt{(\Delta\eta)^2 + (\Delta\varphi)^2} = 1$ where $\Delta\varphi$ is expressed in radians. The jet algorithm is applied in the laboratory frame to all reconstructed particles of the hadronic final state. To prevent the decay particles of the D^* candidate from being attributed to different jets, the D^* candidate is used as a single particle in the jet algorithm, replacing its decay products. In this way the jet containing the D^* meson (D^* jet) is unambiguously defined for each D^* candidate. In events which contain more than one D^* candidate, the jet algorithm is run separately for each candidate, and all candidates for which the dijet selection criteria are fulfilled enter the ΔM distribution. The pseudorapidity of the D^* jet is restricted to the same range as is used for the D^* meson, $|\eta(D^* \text{ jet})| < 1.5$. In addition to the D^* jet a second jet is required. Both jets have to satisfy $p_T(\text{jet}) > 3.5$ GeV. If there is more than one jet that does not contain the D^* meson, the one with the highest $p_T(\text{jet})$ is chosen as the other jet. The pseudorapidity of the other jet has to be in the range $-1.5 < \eta(\text{other jet}) < 2.9$. The invariant mass M_{jj} of the D^* jet and the other jetis required to satisfy $M_{jj} > 6$ GeV in order to select jets from the partons originating from the hard interaction. More details on the selection of the D^*-tagged dijet sample can be found in [52].

The number of D^*-tagged dijet s is extracted from the ΔM distribution of the D^* candidates with the same procedure as used for the inclusive D^* measurement. The ΔM distribution for the selected events in the dijet sample is shown in figure 1b). The fit yields a signal of 3937 ± 114 D^* mesons.

The kinematic range of the inclusive D^* measurement and of the D^*-tagged dijet measurement are summarised in table 3.

5 Cross Section Determination and Systematic Errors

The bin averaged visible differential cross section with respect to a variable Y (with bin width ΔY) is calculated according to

$$\frac{\mathrm{d}\sigma_{vis}(ep \to e\, D^* + X)}{\mathrm{d}Y} = \frac{N(D^*)(1-r)}{\Delta Y \cdot \mathcal{L} \cdot \mathcal{BR} \cdot \epsilon} \tag{1}$$

where $\mathcal{L}$ is the integrated luminosity, $\mathcal{BR}$ is the branching ratio of the analysed decay chain $D^{*\pm} \to D^0 \pi^{\pm}_{slow} \to K^{\mp}\pi^{\pm}\pi^{\pm}_{slow}$ and $(1-r)$ a correction factor to account for reflections from other D^0 decays. The efficiency ϵ includes the detector acceptance, trigger and reconstruction efficiencies and migrations between bins. The contributions of D^* mesons originating from beauty production and from gluon splitting from light flavour production is not subtracted. It is estimated from MC predictions to be below 2%.

inclusive D^* meson and D^*-tagged dijet production	
Photon virtuality	$Q^2 < 2\ \mathrm{GeV}^2$
γp centre-of-mass energy	$100 < W_{\gamma p} < 285\ \mathrm{GeV}$
Pseudorapidity of $D^{*\pm}$	$\vert\eta(D^*)\vert < 1.5$
inclusive D^* meson production	
Transverse momentum of $D^{*\pm}$	$p_T(D^*) > 1.8\ \mathrm{GeV}$
D^*-tagged dijet production	
Transverse momentum of $D^{*\pm}$	$p_T(D^*) > 2.1\ \mathrm{GeV}$
Transverse momentum of D^* jet	$p_T(D^*\ \text{jet}) > 3.5\ \mathrm{GeV}$
Pseudorapidity of D^* jet	$\vert\eta(D^*\ \text{jet})\vert < 1.5$
Transverse momentum of other jet	$p_T(\text{other jet}) > 3.5\ \mathrm{GeV}$
Pseudorapidity of other jet	$-1.5 < \eta(\text{other jet}) < 2.9$
Dijet invariant mass M_{jj}	$M_{jj} > 6\ \mathrm{GeV}$

Table 3: Definition of the kinematic range of the measurements.

The systematic uncertainties are determined in each bin separately and are summarised in table 4 for the total cross section. They are divided into uncertainties which are considered to be uncorrelated between the bins and uncertainties which change the cross section normalisation in all bins. The numbers for the uncertainties listed below are given in per cent of the cross section values.

The following uncorrelated systematic uncertainty sources are considered:

Trigger Efficiency: The simulation of the FTT is verified by a comparison to data in a sample of D^* mesons in deep-inelastic scattering triggered by the scattered electron. For the total inclusive D^* sample the efficiency agrees within a relative uncertainty of 7.5%. This is one of the dominant systematic uncertainties. For the D^*-tagged dijet sample the trigger efficiency is higher, leading to a smaller uncertainty of 3.1% for the total cross section.

Signal Extraction: For the determination of the uncertainty of the signal fit, different parameterisations for the signal and background functions are used. The resulting uncertainty amounts to 1.5%.

D^0 mass cut: The loss of D^* mesons due to the D^0 mass cut is compared between data and simulation as a function of the D^* transverse momentum, assuming a Gaussian resolution for the D^0 mass reconstruction. They agree within 2%, which is assigned as uncertainty.

Reflections: The amount of reflections r from decay modes of the D^0 meson other than $D^0 \to K^\mp\pi^\pm$ amounts to 3.8% in the simulation [53]. It is independent of kinematic quantities within 1%, which is used as systematic uncertainty.

Background from deep inelastic scattering: The background originating from deep inelastic scattering events is estimated with the RAPGAP [54] MC generator. It is found to be below 1%, which is not subtracted but treated as an uncertainty.

dE/dx cut: The efficiency of the cut on the $\mathrm{d}E/\mathrm{d}x$ likelihood of the kaon candidate is studied for data and MC simulation in bins of the transverse momentum of the D^* meson. The relative difference of 1.5% is corrected for in the MC sample. An uncertainty of 0.5% is assigned, covering the possible $p_T(D^*)$ dependence of this correction.

Hadronic energy scale: The energy scale of the hadronic final state has an uncertainty of 2% leading to an uncertainty of the cross section of 0.6% in the inclusive D^* sample and of 2.0% in the D^*-tagged dijet sample.

Model: For the determination of the cross section the PYTHIA and CASCADE predictions are reweighted to describe the data distributions where necessary. For the correction of the data the efficiency from the PYTHIA MC is used. The difference to the efficiency from CASCADE is taken as a systematic uncertainty. It amounts to 2% (1.5%) for the total inclusive D^* (D^*-tagged dijet) cross section.

Fragmentation: The α parameter of the Kartvelishvili function and the position of the $\hat{s}$ threshold are varied within the values given in table 1 resulting in an uncertainty of 2.5% (2.0%) for the total inclusive D^* (D^*-tagged dijet) cross section.

The following normalisation uncertainties are considered:

Track finding efficiency: The systematic uncertainty on the track efficiency of 4.1% per D^* meson arises from two contributions: (i) The comparison of the track finding efficiency in data and simulation leads to an uncertainty of 2% for the slow pion track and 1% for the tracks of the D^0 decay particles, and the uncertainty is assumed to be correlated between the decay particles; (ii) the efficiency with which a track can be fitted to the event vertex leads to a systematic error of 1% per D^* meson. The uncertainty on the track finding efficiency is considered to be half correlated between the bins of the measurement.

Luminosity: The uncertainty on the luminosity measurement for the data sample used in this analysis amounts to 5%.

Branching Ratio: The uncertainty due to the D^* branching ratio is 1.5% [25].

All sources of systematic errors are added in quadrature resulting in a systematic uncertainty of 10.9% (8.5%) for the total cross section of the inclusive D^* (D^*-tagged dijet) production.

6 Results for Inclusive D^* Meson Production

The total visible cross section for D^* meson photoproduction is measured to be:

$$\sigma_{vis}(ep \to e\, D^* + X) = 41.1 \pm 0.8\ (\text{stat.}) \pm 3.6\ (\text{unc.sys.}) \pm 2.7\ (\text{norm.})\ \text{nb} \qquad (2)$$

in the kinematic range defined in table 3. The corresponding predictions from PYTHIA and CASCADE amount to 43.7 nb and 32.9 nb, respectively. Due to the fact that these predictions are based on leading order matrix elements the uncertainty on the normalisation of the cross

Uncertainty source	D^*	D^*-tagged dijet
Uncorrelated uncertainties		
Trigger efficiency	7.5%	3.1%
Signal extraction	1.5%	1.5%
D^0 meson mass cut	2.0%	2.0%
Reflections	1.0%	1.0%
Background from deep-inelastic scattering	1.0%	1.0%
$\mathrm{d}E/\mathrm{d}x$ cut	0.5%	–
Hadronic energy scale	0.6%	2.0%
Model	2.0%	1.5%
Fragmentation	2.5%	2.0%
Track finding efficiency (half)	2.9%	2.9%
Total uncorrelated	9.2%	6.0%
Normalisation uncertainties		
Track finding efficiency (half)	2.9%	2.9%
Luminosity	5.0%	5.0%
Branching ratio	1.5%	1.5%
Total normalisation	6.0%	6.0%
Total	10.9%	8.5%

Table 4: Summary of all sources of systematic uncertainties and their effect on the total D^* and the D^*-tagged dijet production cross section with the breakdown into sources leading to bin-to-bin uncorrelated uncertainties and sources leading to normalisation uncertainties.

sections is large, and is not quantified here. The NLO calculations predict $26\,^{+13}_{-8}$ nb for FMNR, $37\,^{+28}_{-14}$ nb for GMVFNS and $30\,^{+6}_{-7}$ for MC@NLO.

The measured single differential cross section as a function of the transverse momentum $p_T(D^*)$ and the pseudorapidity $\eta(D^*)$ of the D^* meson, the photon-proton centre-of-mass energy $W_{\gamma p}$ and D^* inelasticity $z(D^*)$ are presented in table 5 and in figures 2 and 3. The data are compared to PYTHIA, CASCADE and the NLO predictions of FMNR, GMVFNS and MC@NLO. Since all the predictions have large normalisation uncertainties, the normalised ratio R^{norm} of theory to data is shown in order to compare the shape of the various predictions to the data. R^{norm} is defined as

$$R^{\mathrm{norm}} = \frac{\frac{1}{\sigma_{\mathrm{vis}}^{\mathrm{calc}}} \cdot \frac{\mathrm{d}\sigma^{\mathrm{calc}}}{\mathrm{d}Y}}{\frac{1}{\sigma_{\mathrm{vis}}^{\mathrm{data}}} \cdot \frac{\mathrm{d}\sigma^{\mathrm{data}}}{\mathrm{d}Y}} \tag{3}$$

where $\sigma_{\mathrm{vis}}^{\mathrm{calc}}$ ($\sigma_{\mathrm{vis}}^{\mathrm{data}}$) and $\mathrm{d}\sigma^{\mathrm{calc}}/\mathrm{d}Y$ ($\mathrm{d}\sigma^{\mathrm{data}}/\mathrm{d}Y$) are the total and differential cross section of the model under consideration (of the data), respectively, and Y denotes any measured variable. In this ratio the normalization uncertainties of the data (luminosity, branching ratio and half of the tracking uncertainty) cancel. Similarly, uncertainty sources of the NLO predictions altering the normalisation only do not affect R^{norm} since for each variation the total and the differential cross section are varied simultanously.

The single differential cross sections are compared to the predictions of the LO MC simulations in figure 2. The steep decrease of the cross section with increasing transverse momentum $p_T(D^*)$ is reasonably reproduced by PYTHIA, while CASCADE falls slightly slower than the data. Both MC simulations describe the shape of the observed $\eta(D^*)$ distribution within uncertainties. The cross section decreases as a function of the γp centre-of-mass energy $W_{\gamma p}$, as expected from the photon flux in the equivalent photon approximation [55]. CASCADE predicts a smaller fraction of D^* mesons being produced at small inelasticities $z(D^*)$, similar to what has been observed in deep inelastic scattering at HERA [53]. All distributions are reasonably well described by PYTHIA.

A comparison of the single differential cross sections to the predictions of the NLO calculations is shown in figure 3. For all measured quantities the precision of the measurement presented here is much better than the estimated uncertainty of the NLO calculations. The uncertainty of the NLO predictions is dominated by the variation of the renormalisation scale μ_r, which has a large effect on the absolute cross section, while the differences in the shapes tend to be smaller. Within these large theoretical uncertainties, both the FMNR and GMVFNS predictions agree with the measured cross section as a function of $p_T(D^*)$, while the MC@NLO underestimates the data at small $p_T(D^*)$. The $p_T(D^*)$ shape is best described by the GMVFNS calculation, while FMNR and MC@NLO predict a harder spectrum than observed in data as can be seen in the ratio R^{norm}. The underestimation of the low $p_T(D^*)$ region by the central FMNR and MC@NLO predictions results in a low normalisation in the other distributions. The shape of the $\eta(D^*)$ distribution is reasonably well described by all NLO calculations. All three NLO calculations give a rather precise prediction of the shape of the $W_{\gamma p}$ distribution, which describes the measurement. Given the large uncertainties the predictions for the $z(D^*)$ distribution agree with the data, although when using the central parameter settings for the calculations they differ in shape with respect to data.

Previous H1 and ZEUS analyses of D^* meson photoproduction [1, 3], albeit in different kinematic ranges in the photon virtuality Q^2 and the photon-proton centre-of-mass energy $W_{\gamma p}$, lead to similar conclusions: while all predictions give a good description of the $W_{\gamma p}$ distribution, differences between data and theoretical predictions are observed for variables sensitive to the quantities of the outgoing charm quark.

In order to investigate the correlation between pseudorapidity and transverse momentum, a double differential measurement in $p_T(D^*)$ and $\eta(D^*)$ is performed (table 6). The cross sections of the leading order MCs PYTHIA and CASCADE in the three $p_T(D^*)$ regions shown in figure 4 reflect the different $p_T(D^*)$ dependences seen in figure 2. Both models are in broad agreement with the data. The comparison of the NLO calculations with the data in figure 5 leads to similar conclusions as for the LO MC programs.

7 Results for D^* Tagged Dijet Production

The integrated D^*-tagged dijet cross section in the visible range given in table 3 is measured to be

$$\sigma_{vis}(ep \to e\, D^* \text{ jet} + \text{other jet} + X) = 9.68 \pm 0.28\ (\mathrm{stat.}) \pm 0.51\ (\mathrm{unc.sys.}) \pm 0.64\ (\mathrm{norm.})\ \mathrm{nb}. \quad (4)$$

The corresponding predictions from PYTHIA, CASCADE and MC@NLO amount to $8.9\ \mathrm{nb}$, $8.1\ \mathrm{nb}$ and $7.1\,^{+2.5}_{-1.8}\ \mathrm{nb}$, respectively. In the common range of transverse momentum, $p_T(D^*) > 2.1\ \mathrm{GeV}$, the ratio of the D^*-tagged dijet to the inclusive D^* cross section is $0.304 \pm 0.013 \pm 0.031$, compared to 0.271 and 0.311 for PYTHIA and CASCADE, respectively. MC@NLO predicts a ratio of $0.309\,^{+0.019}_{-0.040}$.

The bin averaged differential cross section for the D^*-tagged dijet production as a function of the transverse momentum p_T and the pseudorapidity η of both the D^* jet and the other jet are listed in table 7 and shown in figures 6 and 7. On average, the other jet is more forward than the D^* jet not only due to the larger measurement range in η, but also within the common region of $-1.5 < \eta < 1.5$. This behaviour is consistent with the expectation that the other jet originates not always from a charm quark. This observation confirms the result of the previous H1 analysis of D^*-tagged dijet photoproduction [3] with improved precision. In figure 6 the measurements are compared to the PYTHIA and the CASCADE predictions. The shapes of the distributions are described well by both models. In figure 7 the measurements are compared to the predictions of MC@NLO. At low transverse momenta of both the D^* jet and the other jet, the predictions lie significantly below the measurement. This results in a smaller total visible cross section which is also observed in the η distribution. The uncertainty band of the MC@NLO prediction includes both variation of the charm mass and variations of the factorisation and renormalisation scales as described in section 2.

In order to investigate further the charm production dynamics, several variables related to the structure of the hadronic final state are studied. The correlation between the jets in the longitudinal and transverse directions is experimentally assessed by the difference in pseudorapidity $\Delta\eta = \eta(\text{other jet}) - \eta(D^* \text{ jet})$ and in the azimuthal angle $|\Delta\varphi|$ between the D^* jet and the other jet. The amount of QCD radiation in addition to the the two leading jets is investigated using the mass variable $M_X = \sqrt{(P + q - (j_1 + j_2))^2}$ with P, q, j_1 and j_2 being the four-vectors of the initial proton, the exchanged photon, the D^* jet and the other jet, respectively. In direct photon processes without radiation, M_X is expected to be close to the proton mass, whereas resolved processes as well as additional QCD radiation will increase M_X. The fraction x_γ of the longitudinal photon momentum entering the hard scattering process can be used to distinguish direct and resolved processes: in collinear factorisation at LO a resolved photon process is characterised by $x_\gamma < 1$, while a direct process has $x_\gamma = 1$. In the D^*-tagged dijet sample, x_γ is approximated by

$$x_\gamma = \frac{\sum_{jets}(E - p_z)_i}{\sum_{HFS}(E - p_z)_j}. \tag{5}$$

The sum in the numerator runs over the particles in the two selected jets, whereas the sum in the denominator contains all reconstructed particles of the hadronic final state.

In table 8 and figures 8 and 9 the bin averaged differential cross sections for the D^*-tagged dijet production as a function of the difference in pseudorapidity $\Delta\eta$ and in azimuthal angle $|\Delta\varphi|$ between the other jet and the D^* jet, the mass M_X and x_γ are presented. The cross section as a function of $\Delta\eta$ is not symmetric because the other jet is on average more forward than the D^* jet. The shape in $\Delta\eta$ is reasonably well described by all QCD calculations. The cross section as a function of $|\Delta\varphi|$ shows a significant contribution away from the back-to-back configuration at $|\Delta\varphi| \simeq 180°$. Such a configuration can be described by models which include significant contributions from higher order QCD radiation or a transverse momentum of the gluon in the initial state. Whereas PYTHIA predicts a too small relative contribution of these configurations, CASCADE overestimates them. The prediction from MC@NLO, shown in figure 9b), agrees well in shape with the measurement.

The cross section as a function of the invariant mass M_X is reasonably well described by the predictions of CASCADE and PYTHIA in the region of $M_X < 120$ GeV, whereas the measured cross section is larger than the predictions for the highest M_X bin. The large M_X region is correlated with the region of small x_γ, where also the predictions are below the measurement. MC@NLO predicts a different shape for M_X and is not able to describe the shape of the x_γ distribution.

The $|\Delta\varphi|$ dependence of the cross sections in two regions of x_γ is presented in table 9 and in figure 10. PYTHIA is in agreement with the data. CASCADE overestimates the contribution from small $|\Delta\varphi|$ in both x_γ regions. MC@NLO describes the shape well in the region of small x_γ, where resolved photon processes are enhanced, but is too low in normalisation. At large x_γ values MC@NLO predicts the size of the cross section correctly, but overestimates the contribution from small $|\Delta\varphi|$.

The cross sections for D^*-tagged dijet production show that in general both hard partons in the final state can be described reasonably well by the QCD predictions, while the details and especially the correlations between the D^* jet and the other jet are not described very well by these theoretical calculations.

8 Conclusions

The production of D^* mesons in the photoproduction regime is investigated with the H1 detector at HERA with a seven times larger signal sample compared to the previous H1 measurement. The events containing D^* mesons were triggered by the tracks of the decay particles in the channel $D^\pm \to D^0\pi^\pm_{slow} \to K^\mp\pi^\pm\pi^\pm_{slow}$. Single and double differential cross sections are measured, and the results are compared to leading order QCD models provided by the MC simulation programs PYTHIA and CASCADE and to the next-to-leading order pQCD calculations FMNR, GMVFNS and MC@NLO. The precision of the cross section measurements far exceeds the predictive power of the NLO theories. The shapes of the differential cross sections, however, are less sensitive to the theoretical uncertainties, and generally show reasonable agreement with the data.

The cross section for D^*-tagged dijet production is measured and compared to predictions of PYTHIA, CASCADE and MC@NLO. The results are consistent with the expectation that the non-D^*-jet can originate not only from a charm quark but also from a light parton. Significant contributions from higher order QCD radiation or transverse momenta of the partons in the initial state are needed to describe the cross section away from the back-to-back configuration between the D^* jet and other jet at $|\Delta\varphi| \simeq 180°$. The cross sections as a function of the transverse momentum and the pseudorapidity of the D^* jet and the other jet are reasonably well described by the predictions. However, significant differences are observed in the description of some variables related to the structure of the hadronic final state, such as $|\Delta\varphi|$, M_X and x_γ.

Acknowledgements

We are grateful to the HERA machine group whose outstanding efforts have made this experiment possible. We thank the engineers and technicians for their work in constructing and maintaining the H1 detector, our funding agencies for financial support, the DESY technical staff for continual assistance and the DESY directorate for support and for the hospitality which they extend to the non-DESY members of the collaboration.

References

[1] J. Breitweg *et al.* [ZEUS Collaboration], Eur. Phys. J. **C6** (1999) 67 [hep-ex/9807008].

[2] C. Adloff *et al.* [H1 Collaboration], Nucl. Phys. **B545** (1999) 21 [hep-ex/9812023].

[3] A. Aktas *et al.* [H1 Collaboration], Eur. Phys. J. **C50** (2007) 251 [hep-ex/0608042].

[4] S. Chekanov *et al.* [ZEUS Collaboration], Phys. Lett. **B565** (2003) 87 [hep-ex/0302025].

[5] S. Chekanov *et al.* [ZEUS Collaboration], Nucl. Phys. **B729** (2005) 492 [hep-ex/0507089].

[6] A. Aktas *et al.* [H1 Collaboration], Phys. Lett. **B621** (2005) 56 [hep-ex/0503038].

[7] V.N. Gribov and L.N. Lipatov, Sov. J. Nucl. Phys. **15** (1972) 675 [Yad. Fiz. **15** (1972) 1218];
V.N. Gribov and L.N. Lipatov, Sov. J. Nucl. Phys. **15** (1972) 438 [Yad. Fiz. **15** (1972) 781];
L.N. Lipatov, Sov. J. Nucl. Phys. **20** (1975) 94 [Yad. Fiz. **20** (1974) 181];
Y.L. Dokshitzer, Sov. Phys. JETP **46** (1977) 641 [Zh. Eksp. Teor. Fiz. **73** (1977) 1216];
G. Altarelli and G. Parisi, Nucl. Phys. **B126** (1977) 298.

[8] M. Ciafaloni, Nucl. Phys. **B296** (1988) 49;
S. Catani, F. Fiorani and G. Marchesini, Phys. Lett. **B234** (1990) 339;
S. Catani, F. Fiorani and G. Marchesini, Nucl. Phys. **B336** (1990) 18;
G. Marchesini, Nucl. Phys. **B445** (1995) 49 [hep-ph/9412327].

[9] J. Collins and H. Jung, Proceedings of "HERA and the LHC", eds. H. Jung and A. De Roeck, CERN-2005-014, DESY-PROC-2005-001 (2005) 261 [hep-ph/0508280].

[10] W.K. Tung, S. Kretzer and C. Schmidt, J. Phys. **G28** (2002) 983 [hep-ph/0110247].

[11] R. Brun *et al.*, GEANT3, Technical Report CERN-DD/EE-81-1 (1987).

[12] T. Sjöstrand *et al.*, PYTHIA 6.1, Comp. Phys. Commun.**135** (2001) 238 [hep-ph/0010017].

[13] B. Andersson, G. Gustafson and B. Söderberg, Z. Phys. **C20** (1983) 317;
B. Andersson, G. Gustafson, G. Ingelman and T. Sjöstrand, Phys. Rept. **97** (1983) 31.

[14] M. G. Bowler, Z. Phys. **C11** (1981) 169.

[15] V. Kartvelishvili, A. Likhoded and V. Petrov, Phys. Lett. **B78** (1978) 615.

[16] F. D. Aaron *et al.* [H1 Collaboration], Eur. Phys. J. **C59** (2009) 589 [arXiv:0808.1003].

[17] J. Pumplin *et al.*, JHEP **0207** (2002) 012 [hep-ph/0201195].

[18] M. Glück, E. Reya and A. Vogt, Phys. Rev. **D45** (1992) 3986;
M. Glück, E. Reya and A. Vogt, Phys. Rev. **D46** (1992) 1973.

[19] H. Jung *et al.*, CASCADE 2.2, Eur. Phys. J. **C70** (2010) 1237 [arXiv:1008.0152].

[20] H. Jung, Proceedings of "XII International Workshop on Deep-Inelastic Scattering (DIS 2004)", eds. D. Bruncko, J. Ferencei and P. Stríženec, (2004) 299 [hep-ph/0411287].

[21] S. Frixione, P. Nason and G. Ridolfi, Nucl. Phys. **B454** (1995) 3 [hep-ph/9506226].

[22] S. Frixione, M.L. Mangano, P. Nason and G. Ridolfi, Phys. Lett. **B348** (1995) 633 [hep-ph/9412348].

[23] F. D. Aaron *et al.* [H1 and ZEUS Collaboration], JHEP **1001** (2010) 109 [arXiv:0911.0884].

[24] H.L. Lai *et al.* [CTEQ Collaboration], Eur. Phys. J. **C12** (2000) 375 [hep-ph/9903282].

[25] K. Nakamura *et al.* [Particle Data Group], J. Phys. **G37** (2010) 075021.

[26] G. Kramer and H. Spiesberger, Eur. Phys. J. **C38** (2004) 309 [hep-ph/0311062].

[27] B.A. Kniehl, G. Kramer, I. Schienbein and H. Spiesberger, Eur. Phys. J. **C62** (2009) 365 [arXiv:0902.3166].

[28] T. Kneesch, B.A. Kniehl, G. Kramer and I. Schienbein, Nucl. Phys. **B799** (2008) 34 [arXiv:0712.0481].

[29] P. Aurenche, M. Fontannaz and J.P. Guillet, Eur. Phys. J. **C44** (2005) 395 [hep-ph/0503259].

[30] S. Frixione and B.R. Webber, JHEP **0206** (2002) 029 [hep-ph/0204244];
S. Frixione, P. Nason and B.R. Webber, JHEP **0308** (2003) 007 [hep-ph/0305252].

[31] T. Toll and S. Frixione, Phys. Lett. **B703** (2011) 452 [arXiv:1106.1614].

[32] G. Corcella *et al.*, JHEP **0101** (2001) 010 [hep-ph/0011363].

[33] L. Gladilin, hep-ex/9912064.

[34] I. Abt *et al.* [H1 Collaboration], Nucl. Instrum. Methods **A386** (1997) 310;

I. Abt *et al.* [H1 Collaboration], Nucl. Instrum. Methods **A386** (1997) 348.

[35] D. Pitzl *et al.*, Nucl. Instrum. Methods **A454** (2000) 334 [hep-ex/0002044];

B. List, Nucl. Instrum. Methods **A501** (2001) 49.

[36] J. Becker *et al.*, Nucl. Instrum. Methods **A586** (2008) 190 [physics/0701002].

[37] C. Kleinwort, Proceedings of "First LHC Detector Alignment Workshop", eds. S. Blusk *et al.*, CERN-2007-004 (2007) 41.

[38] A. Baird *et al.*, IEEE Trans. Nucl. Sci. **48** (2001) 1276 [hep-ex/0104010];

D. Meer *et al.*, IEEE Trans. Nucl. Sci. **49** (2002) 357 [hep-ex/0107010].

[39] N.E. Berger, "Measurement of Diffractive ϕ Meson Photoproduction at HERA with the H1 Fast Track Trigger", Ph.D. thesis, ETH Zürich (2007), ETHZ-IPP Internal Report 2007-01 (available at http://www-h1.desy.de/publications/theses_list.html).

[40] A.W. Jung, "Measurement of the $D^{*\pm}$ Meson Cross Section and Extraction of the Charm Contribution, $F_2^c(x, Q^2)$, to the Proton Structure in Deep Inelastic ep Scattering with the H1 Detector at HERA", Ph.D. thesis, Univ. Heidelberg (2009), HD-KIP-09-01, DESY-THESIS-2009-001
(available at http://www-h1.desy.de/publications/theses_list.html).

[41] B. Andrieu *et al.* [H1 Calorimeter Group], Nucl. Instrum. Methods **A344** (1994) 492;

B. Andrieu *et al.* [H1 Calorimeter Group], Nucl. Instrum. Methods **A350** (1994) 57.

[42] R.-D. Appuhn *et al.* [H1 SpaCal Group], Nucl. Instrum. Methods **A386** (1997) 397.

[43] T. Nicholls *et al.* [H1 SpaCal Group], Nucl. Instrum. Methods **A374** (1996) 149.

[44] M. Peez, "Search for deviations from the Standard Model in high transverse energy processes at the electron-proton collider HERA", Ph.D. thesis, Univ. Lyon (2003), DESY-THESIS-2003-023
(available at http://www-h1.desy.de/publications/theses_list.html);

S. Hellwig, "Untersuchung der $D^* - \pi_{slow}$ Double Tagging Methode in Charmanalysen", Dipl. thesis, Univ. Hamburg (2004)
(available at http://www-h1.desy.de/publications/theses_list.html).

[45] A. Blondel and F. Jacquet, Proceedings of "The Study of an ep Facility for Europe", ed. U. Amaldi, DESY 79/48 (1979) 391.

[46] G. J. Feldman *et al.*, Phys. Rev. Lett.**38** (1977) 1313.

[47] J.E. Gaiser, "Charmonium Spectroscopy from Radiative Decays of the J/ψ and ψ'", Ph.D. thesis, Stanford University (1982).

[48] P. Granet *et al.* [French-Soviet Collaboration], Nucl. Phys. **B140** (1978) 389.

[49] W. Verkerke and D. Kirkby, “The RooFit toolkit for data modeling”, User Manual, 2006, avaiable at http://roofit.sourceforge.net.

[50] E. Hennekemper, “Simulation and Calibration of the Specific Energy Loss of the Central Jet Chambers of the H1 Detector and Measurement of the Inclusive $D^{*\pm}$ Meson Cross Section in Photoproduction at HERA”, Ph.D. thesis, Univ. Heidelberg (2011), HD-KIP-11-68
(available at http://www-h1.desy.de/publications/theses_list.html).

[51] S.D. Ellis and D.E. Soper, Phys. Rev. **D48** (1993) 3160 [hep-ph/9305266].

[52] Z. Staykova, “Measurement of D^* Meson with Two Jets in Photoproduction with the H1 Detector at HERA”, Ph.D. thesis, Univ. Hamburg (2010), DESY-THESIS-2011-002
(available at http://www-h1.desy.de/publications/theses_list.html).

[53] F.D. Aaron *et al.* [H1 Collaboration], Eur. Phys. J. **C71** (2011) 1769 [arXiv:1106.1028].

[54] H. Jung, RAPGAP 3.1, Comp. Phys. Commun.**86** (1995) 147.

[55] C.F. von Weizsäcker, Z. Phys. **88** (1934) 612;
E.J. Williams, Phys. Rev. **45** (1934) 729;
V.M. Budnev, I.F. Ginzburg, G.V. Meledin and V.G. Serbo, Phys. Rept. **15** (1975) 181.

H1 inclusive D^* cross sections				
$p_T(D^*)$ range [GeV]		$\mathrm{d}\sigma/\mathrm{d}p_T(D^*)$ [nb/GeV]	stat. [%]	sys. [%]
1.8	2.1	36	±12	±13
2.1	2.5	29	±8	±13
2.5	3.0	15	±5	±11
3.0	3.5	8.6	±6	±8
3.5	4.5	4.3	±3	±8
4.5	5.5	2.3	±4	±9
5.5	6.5	0.89	±5	±7
6.5	9.0	0.25	±6	±8
9.0	12.5	0.047	±12	±11
$\eta(D^*)$ range		$\mathrm{d}\sigma/\mathrm{d}\eta(D^*)$ [nb]	stat. [%]	sys. [%]
-1.5	-1.0	13	±5	±10
-1.0	-0.5	16	±4	±10
-0.5	0.0	18	±4	±10
0.0	0.5	15	±4	±10
0.5	1.0	12	±5	±10
1.0	1.5	7.9	±10	±10
$W_{\gamma p}$ range [GeV]		$\mathrm{d}\sigma/\mathrm{d}(W_{\gamma p})$ [nb/GeV]	stat. [%]	sys. [%]
100	140	0.34	±3	±10
140	180	0.29	±3	±10
180	230	0.19	±4	±10
230	285	0.11	±6	±10
$z(D^*)$ range		$\mathrm{d}\sigma/\mathrm{d}(z(D^*))$ [nb]	stat. [%]	sys. [%]
0.00	0.10	45	±14	±11
0.10	0.20	89	±5	±11
0.20	0.35	76	±3	±10
0.35	0.55	55	±3	±9
0.55	1.00	13	±4	±11

Table 5: Bin averaged single differential cross sections for inclusive D^* production in bins of $p_T(D^*)$, $\eta(D^*)$, $W_{\gamma p}$ and $z(D^*)$ with their statistical and uncorrelated systematic uncertainties. The normalisation uncertainty of 6.0% is not included.

H1 inclusive D^* cross sections				
$1.8 \leq p_T(D^*) < 2.5$ GeV				
$\eta(D^*)$ range		$\mathrm{d}^2\sigma/\mathrm{d}\eta\mathrm{d}p_T$ [nb/GeV]	stat. [%]	sys. [%]
-1.5	-1.0	13	± 12	± 14
-1.0	-0.5	12	± 12	± 14
-0.5	0.0	14	± 11	± 13
0.0	0.5	10	± 16	± 13
0.5	1.5	7.8	± 18	± 13
$2.5 \leq p_T(D^*) < 4.5$ GeV				
$\eta(D^*)$ range		$\mathrm{d}^2\sigma/\mathrm{d}\eta\mathrm{d}p_T$ [nb/GeV]	stat. [%]	sys. [%]
-1.5	-1.0	2.2	± 6	± 9
-1.0	-0.5	3.0	± 4	± 9
-0.5	0.0	3.6	± 5	± 9
0.0	0.5	3.0	± 5	± 9
0.5	1.0	2.3	± 7	± 9
1.0	1.5	1.8	± 14	± 9
$4.5 \leq p_T(D^*) < 12.5$ GeV				
$\eta(D^*)$ range		$\mathrm{d}^2\sigma/\mathrm{d}\eta\mathrm{d}p_T$ [nb/GeV]	stat. [%]	sys. [%]
-1.5	-1.0	0.070	± 10	± 12
-1.0	-0.5	0.14	± 6	± 11
-0.5	0.0	0.22	± 6	± 11
0.0	0.5	0.24	± 5	± 11
0.5	1.0	0.18	± 6	± 11
1.0	1.5	0.11	± 10	± 12

Table 6: Bin averaged double differential cross sections for inclusive D^* production in bins of $\eta(D^*)$ for three ranges in $p_T(D^*)$ with their statistical and uncorrelated systematic uncertainties. The normalisation uncertainty of 6.0% is not included.

H1 D^*-tagged dijet cross sections				
$\eta(D^*$ jet$)$ range		$\mathrm{d}\sigma/\mathrm{d}\eta(D^*$ jet$)$ [nb]	stat. [%]	sys. [%]
-1.5	-1.0	2.3	±12	±11
-1.0	-0.5	3.2	±7	±8
-0.5	0.0	3.9	±7	±8
0.0	0.5	3.9	±8	±8
0.5	1.0	3.4	±9	±8
1.0	1.5	2.8	±14	±8
$\eta($other jet$)$ range		$\mathrm{d}\sigma/\mathrm{d}\eta($other jet$)$ [nb]	stat. [%]	sys. [%]
-1.5	-1.0	1.2	±15	±11
-1.0	-0.5	1.3	±13	±9
-0.5	0.0	2.1	±10	±8
0.0	0.5	2.6	±9	±8
0.5	1.0	2.7	±8	±8
1.0	1.5	2.9	±8	±8
1.5	2.2	2.5	±10	±8
2.2	2.9	2.2	±15	±8
$p_T(D^*$ jet$)$ range [GeV]		$\mathrm{d}\sigma/\mathrm{d}p_T(D^*$ jet$)$ [nb/GeV]	stat. [%]	sys. [%]
3.5	5.0	2.7	±8	±8
5.0	8.0	1.4	±5	±7
8.0	15.0	0.17	±7	±7
$p_T($other jet$)$ range [GeV]		$\mathrm{d}\sigma/\mathrm{d}p_T($other jet$)$ [nb/GeV]	stat. [%]	sys. [%]
3.5	5.0	3.0	±7	±8
5.0	8.0	1.2	±5	±7
8.0	15.0	0.24	±7	±10

Table 7: Bin averaged single differential cross sections for D^*-tagged dijet production in bins of η and p_T of the D^* jet and the other jet with their statistical and uncorrelated systematic uncertainties. The normalisation uncertainty of 6.0% is not included.

H1 D^*-tagged dijet cross sections				
$\Delta\eta$ range		$\mathrm{d}\sigma/\mathrm{d}\Delta\eta$ [nb]	stat. [%]	sys. [%]
-3.0	-2.0	0.24	± 33	± 13
-2.0	-1.0	0.85	± 12	± 9
-1.0	0.0	1.7	± 9	± 8
0.0	1.0	2.4	± 7	± 8
1.0	2.0	2.5	± 7	± 8
2.0	3.0	1.6	± 11	± 8
3.0	4.0	0.63	± 21	± 12
4.0	4.4	0.22	± 79	± 31
$\|\Delta\varphi\|$ range [deg.]		$\mathrm{d}\sigma/\mathrm{d}\|\Delta\varphi\|$ [nb/deg.]	stat. [%]	sys. [%]
0	110	0.0066	± 24	± 8
110	150	0.057	± 8	± 8
150	170	0.20	± 5	± 7
170	180	0.28	± 6	± 8
M_X range [GeV]		$\mathrm{d}\sigma/\mathrm{d}M_X$ [nb/GeV]	stat. [%]	sys. [%]
30	75	0.075	± 4	± 7
75	120	0.069	± 7	± 7
120	250	0.024	± 11	± 7
x_γ range		$\mathrm{d}\sigma/\mathrm{d}x_\gamma$ [nb]	stat. [%]	sys. [%]
0.00	0.45	4.9	± 15	± 9
0.45	0.75	11	± 7	± 8
0.75	1.00	17	± 4	± 7

Table 8: Bin averaged single differential cross sections for D^*-tagged dijet production in bins of $\Delta\eta$, $|\Delta\varphi|$, x_γ and M_X with their statistical and uncorrelated systematic uncertainties. The normalisation uncertainty of 6.0% is not included.

H1 D^*-tagged dijet cross sections				
$x_\gamma < 0.75$				
$\|\Delta\varphi\|$ range [deg.]		$\mathrm{d}\sigma/\mathrm{d}\|\Delta\varphi\|$ [nb/deg.]	stat. [%]	sys. [%]
0	110	0.0057	± 28	± 9
110	150	0.040	± 12	± 9
150	170	0.10	± 10	± 9
170	180	0.12	± 13	± 10
$x_\gamma \geq 0.75$				
$\|\Delta\varphi\|$ range [deg.]		$\mathrm{d}\sigma/\mathrm{d}\|\Delta\varphi\|$ [nb/deg.]	stat. [%]	sys. [%]
0	110	0.0009	± 34	± 12
110	150	0.017	± 11	± 8
150	170	0.097	± 6	± 8
170	180	0.16	± 6	± 9

Table 9: Bin averaged single differential cross sections for D^*-tagged dijet production in bins of $|\Delta\varphi|$ in two regions of x_γ with their statistical and uncorrelated systematic uncertainties. The normalisation uncertainty of 6.0% is not included.

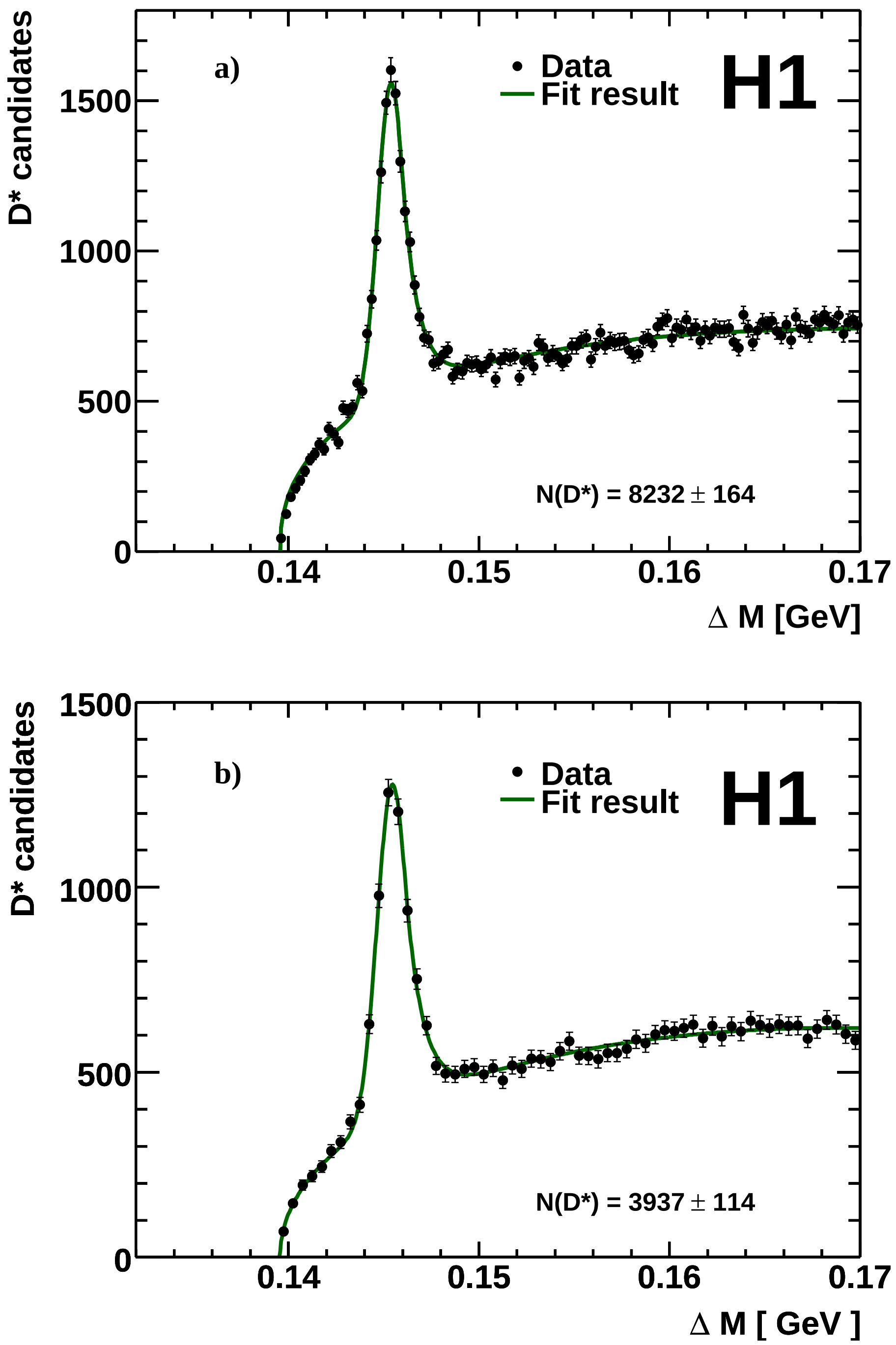

Figure 1: Distribution of ΔM for D^* candidates a) in the inclusive D^* sample and b) in the D^* tagged dijet sample. The fit function is also shown.

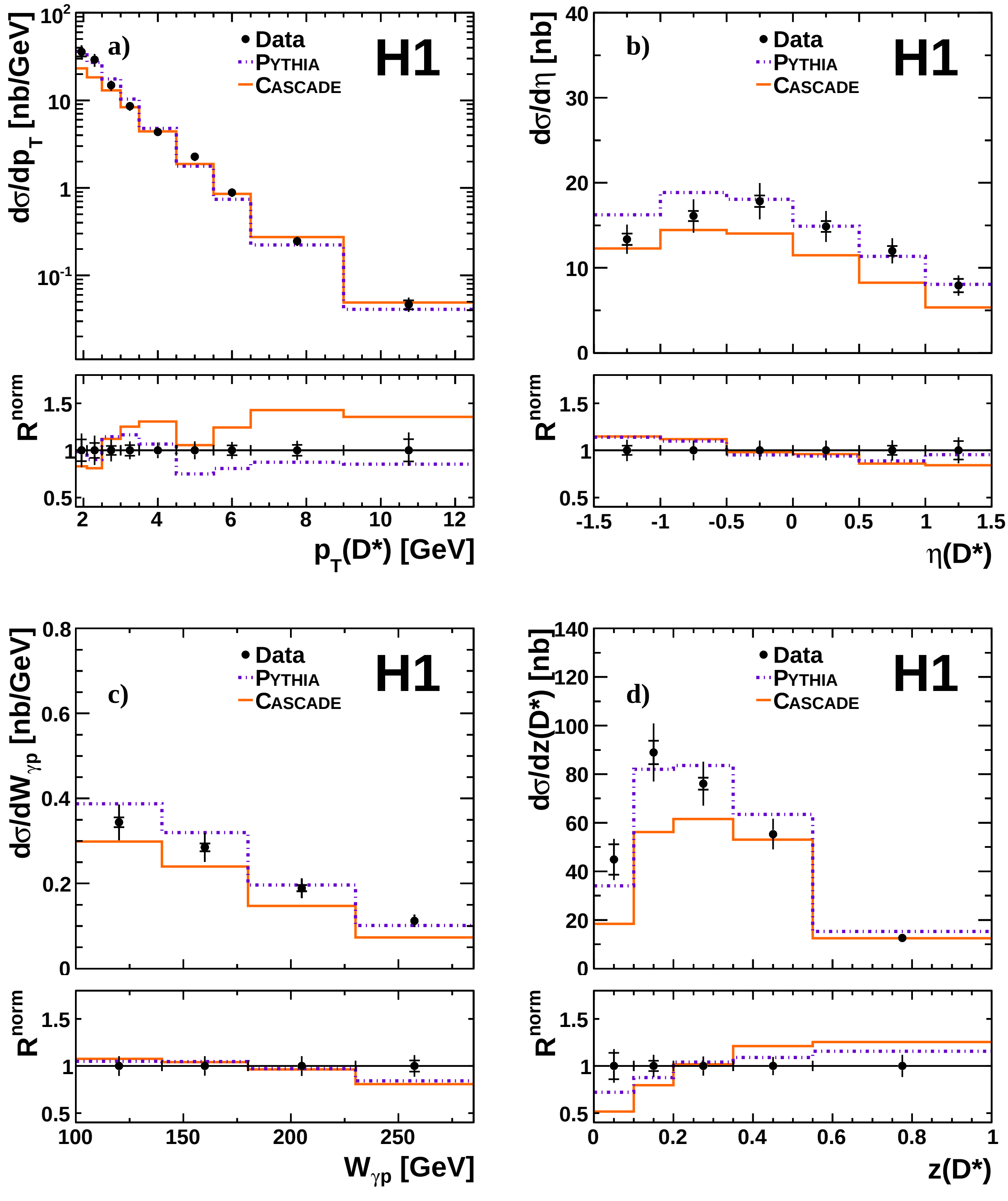

Figure 2: Single differential D^* cross section as a function of $p_T(D^*)$, $\eta(D^*)$, $W_{\gamma p}$, and $z(D^*)$ compared to PYTHIA and CASCADE predictions. Here and in the following figures the inner error bar depicts the statistical error and the outer shows the statistical, and uncorrelated systematic and normalisation uncertainty added in quadrature. The normalised ratio R^{norm} (see text) is also shown.

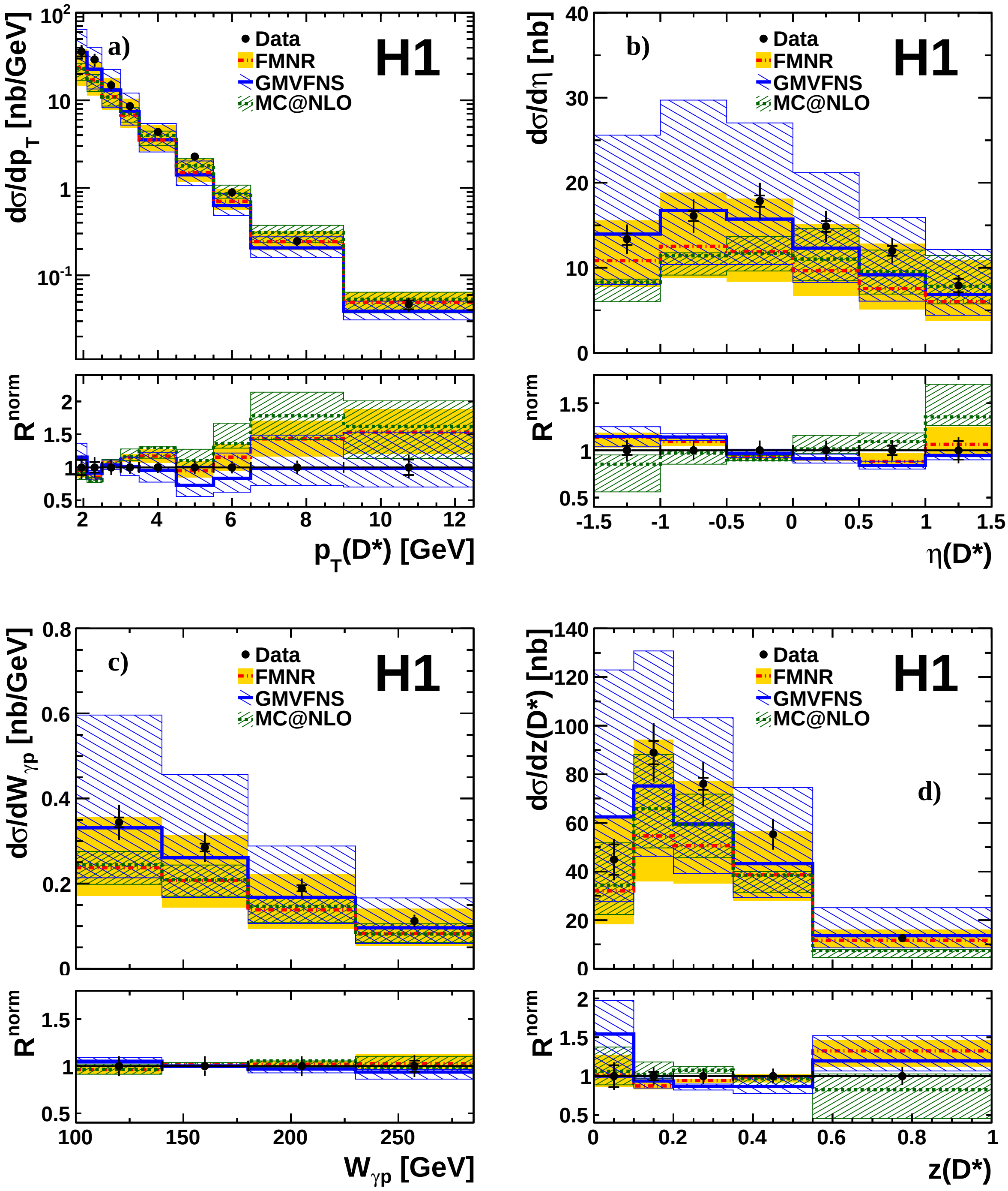

Figure 3: Single differential D^* cross section as a function of $p_T(D^*)$, $\eta(D^*)$, $W_{\gamma p}$, and $z(D^*)$ compared to the next-to-leading order predictions of FMNR, GMVFNS and MC@NLO. The normalised ratio R^{norm} (see text) is also shown.

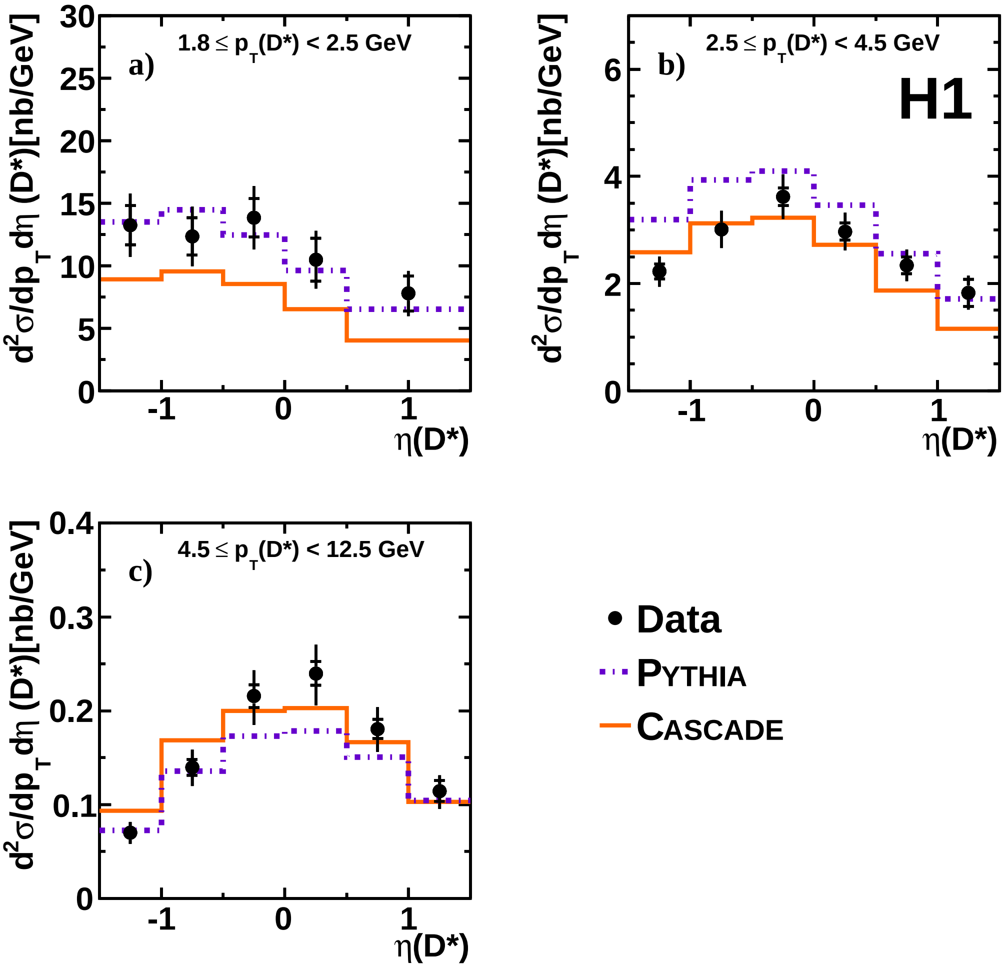

Figure 4: Double differential D^* cross section as a function of $\eta(D^*)$ for three bins of $p_T(D^*)$ compared to PYTHIA and CASCADE predictions.

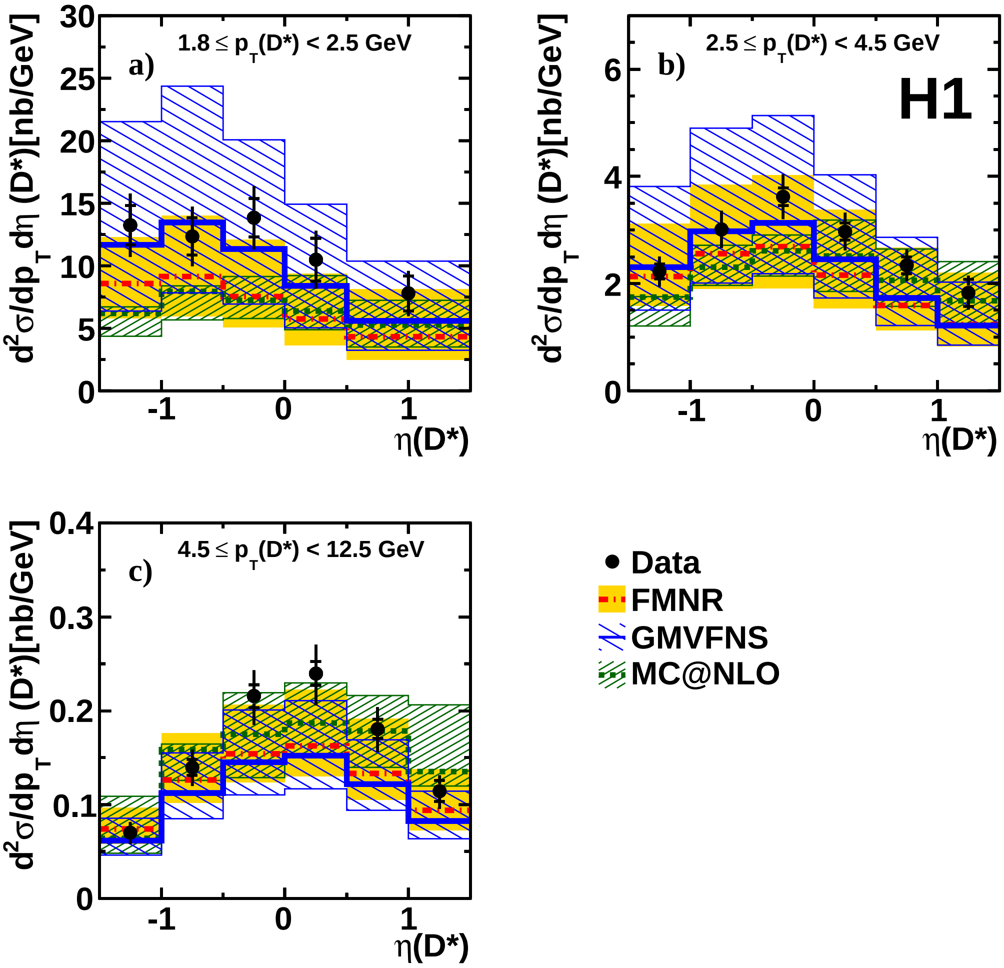

Figure 5: Double differential D^* cross section as a function of $\eta(D^*)$ for three bins of $p_T(D^*)$ compared to the next-to-leading order predictions of FMNR, GMVFNS and MC@NLO.

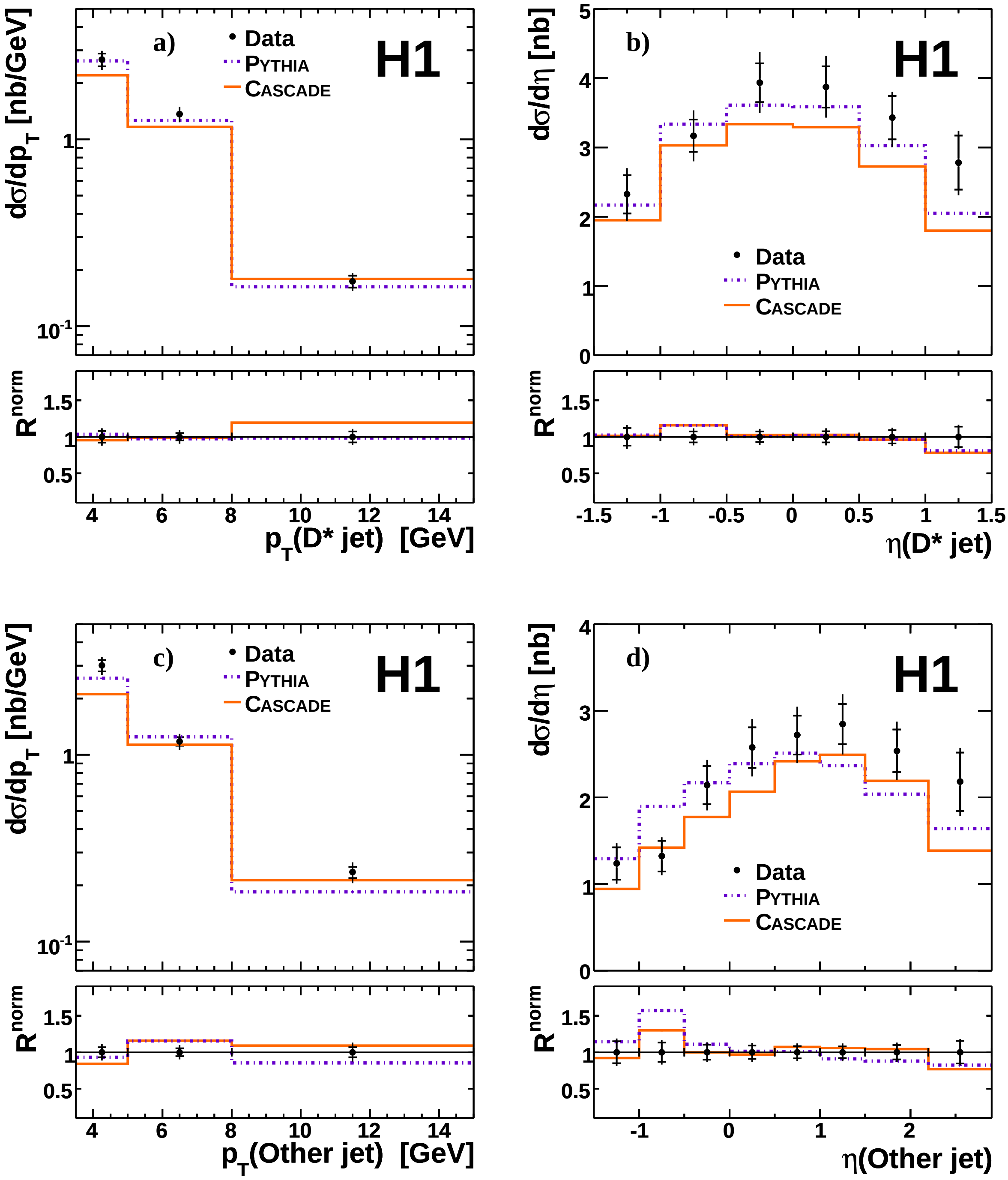

Figure 6: Single differential cross section for D^*-tagged dijet production as a function of p_T and η of the D^* jet and the other jet compared to PYTHIA and CASCADE predictions. The normalised ratio $R^{\rm norm}$ (see text) is also shown.

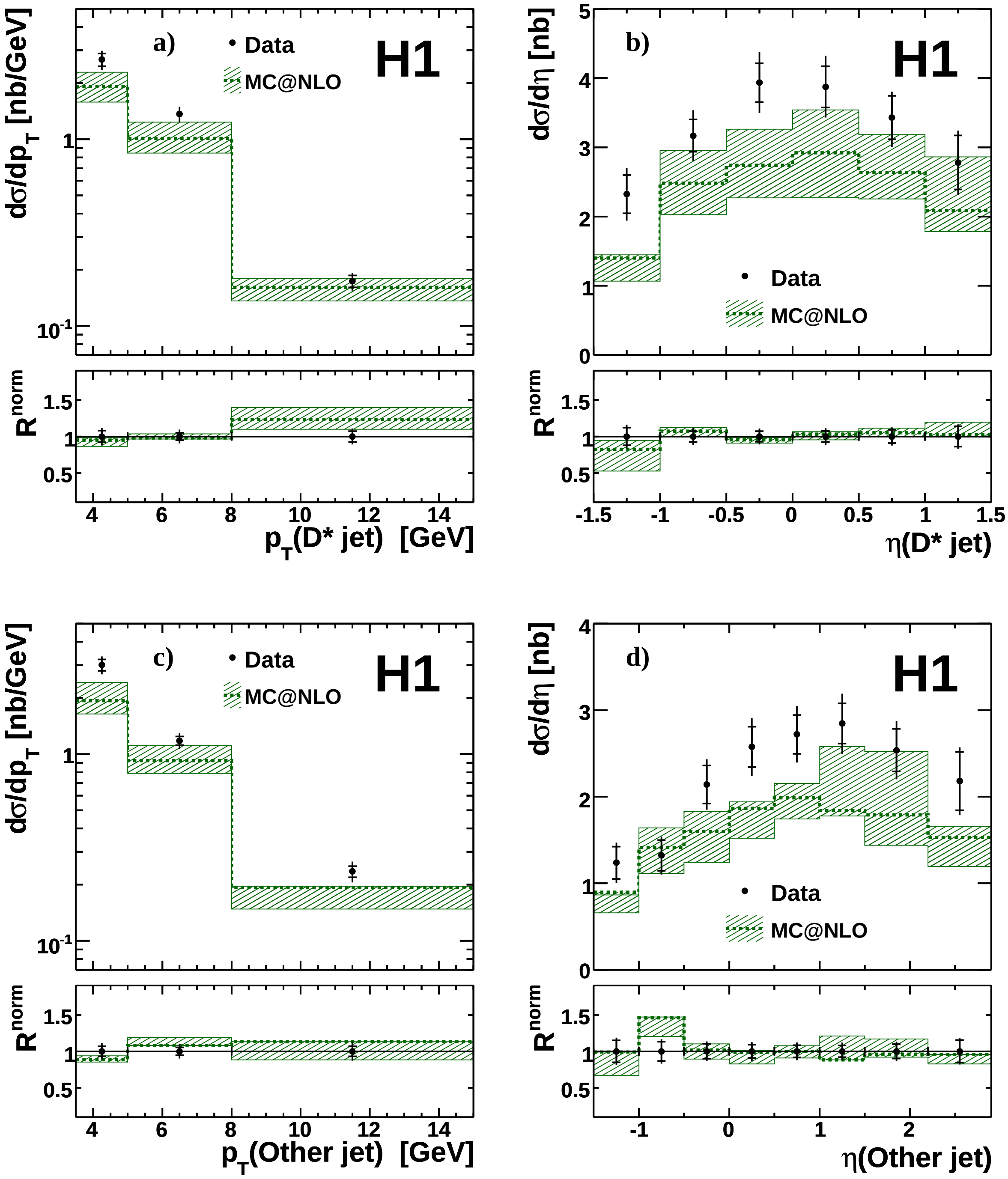

Figure 7: Single differential cross section for D^*-tagged dijet production as a function of p_T and η of the D^* jet and the other jet compared to MC@NLO predictions. The normalised ratio R^{norm} (see text) is also shown.

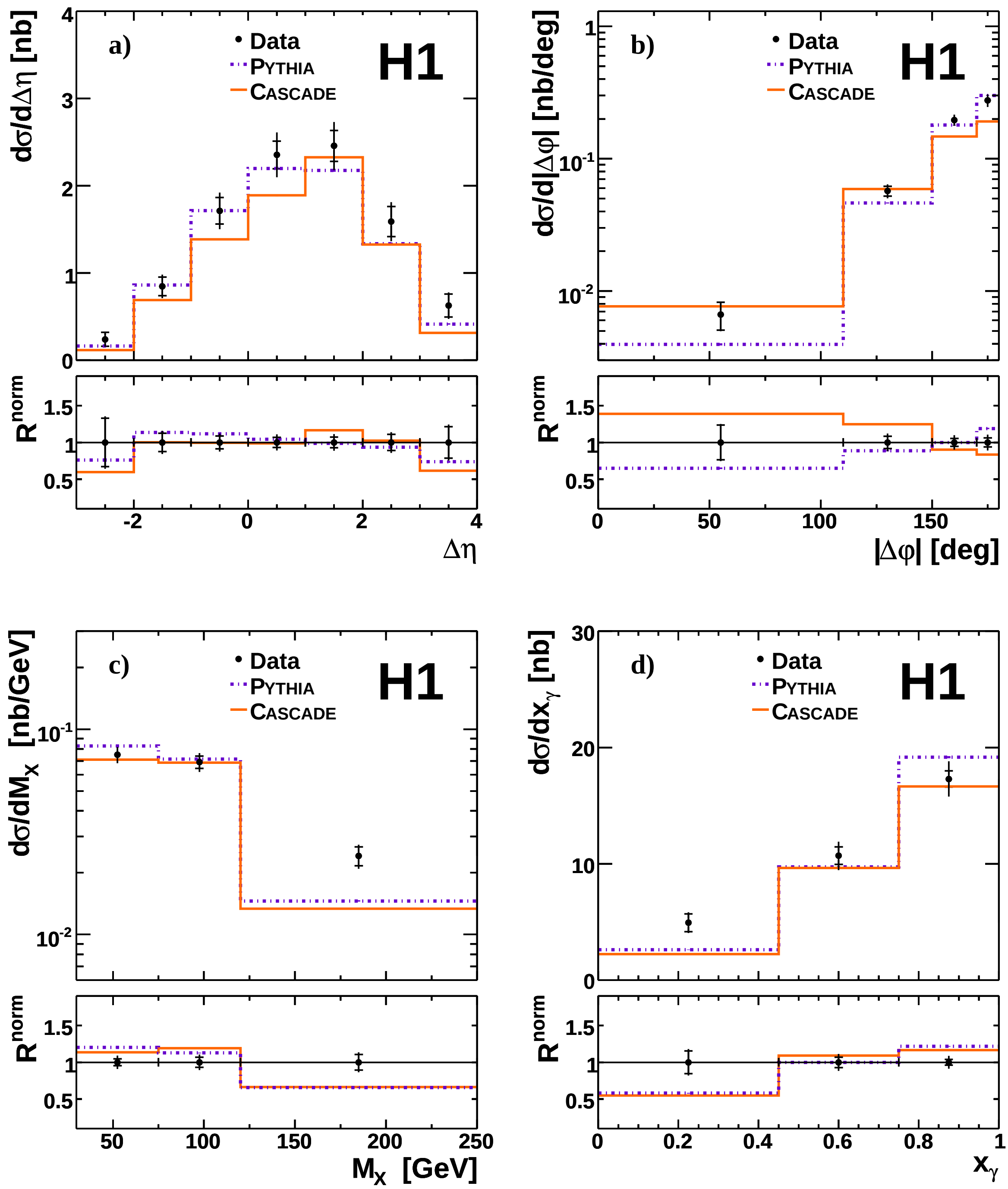

Figure 8: Single differential cross section for D^*-tagged dijet production as a function of the difference in pseudorapidity $\Delta\eta$ and in azimuthal angle $\Delta\varphi$ between the other jet and the D^* jet, the mass M_X and x_γ compared to PYTHIA and CASCADE predictions. The normalised ratio $R^{\rm norm}$ (see text) is also shown.

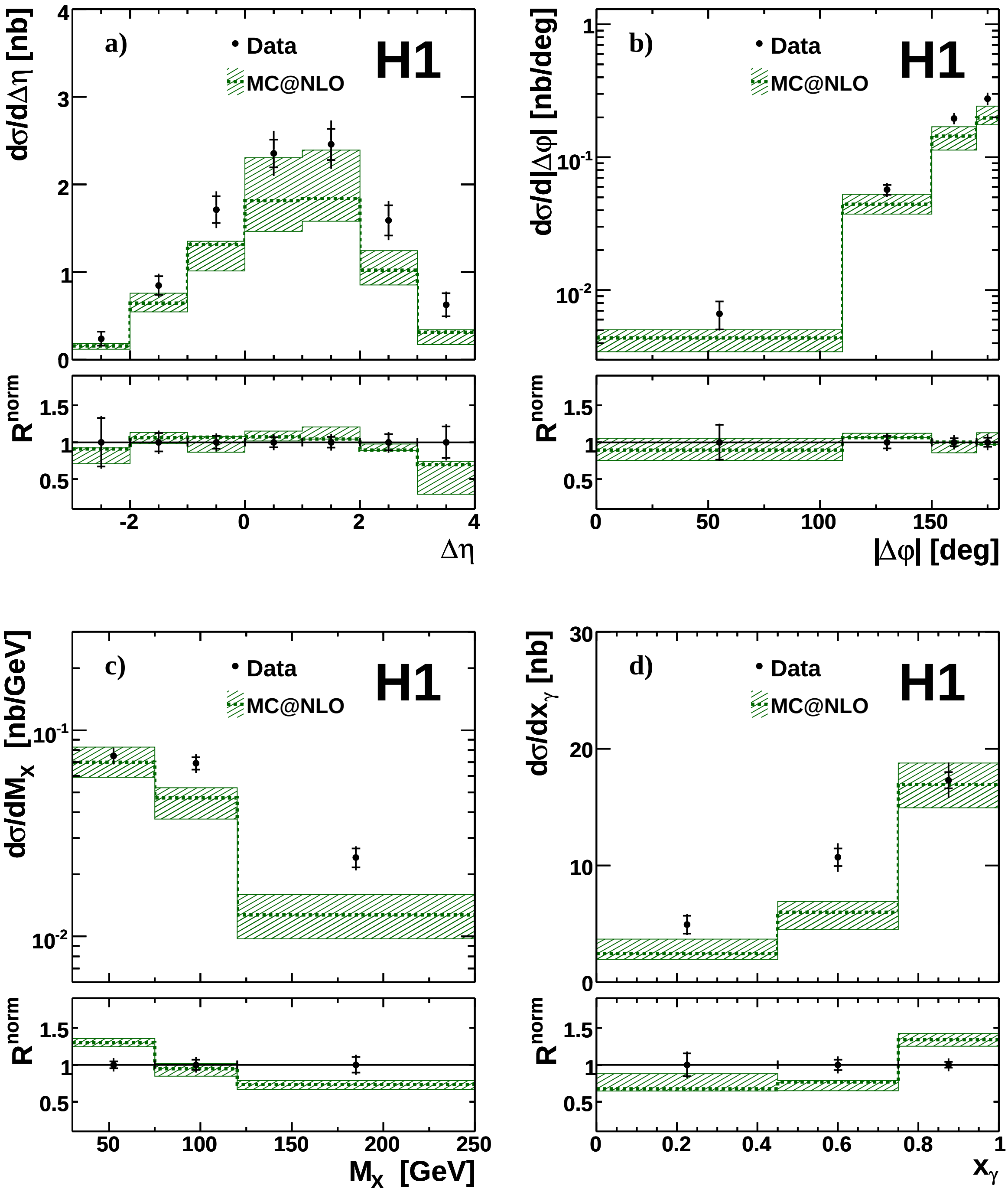

Figure 9: Single differential cross section for D^*-tagged dijet production as a function of the difference in pseudorapidity $\Delta\eta$ and in azimuthal angle $\Delta\varphi$ between the other jet and the D^* jet, the mass M_X and x_γ compared to MC@NLO predictions. The normalised ratio R^{norm} (see text) is also shown.

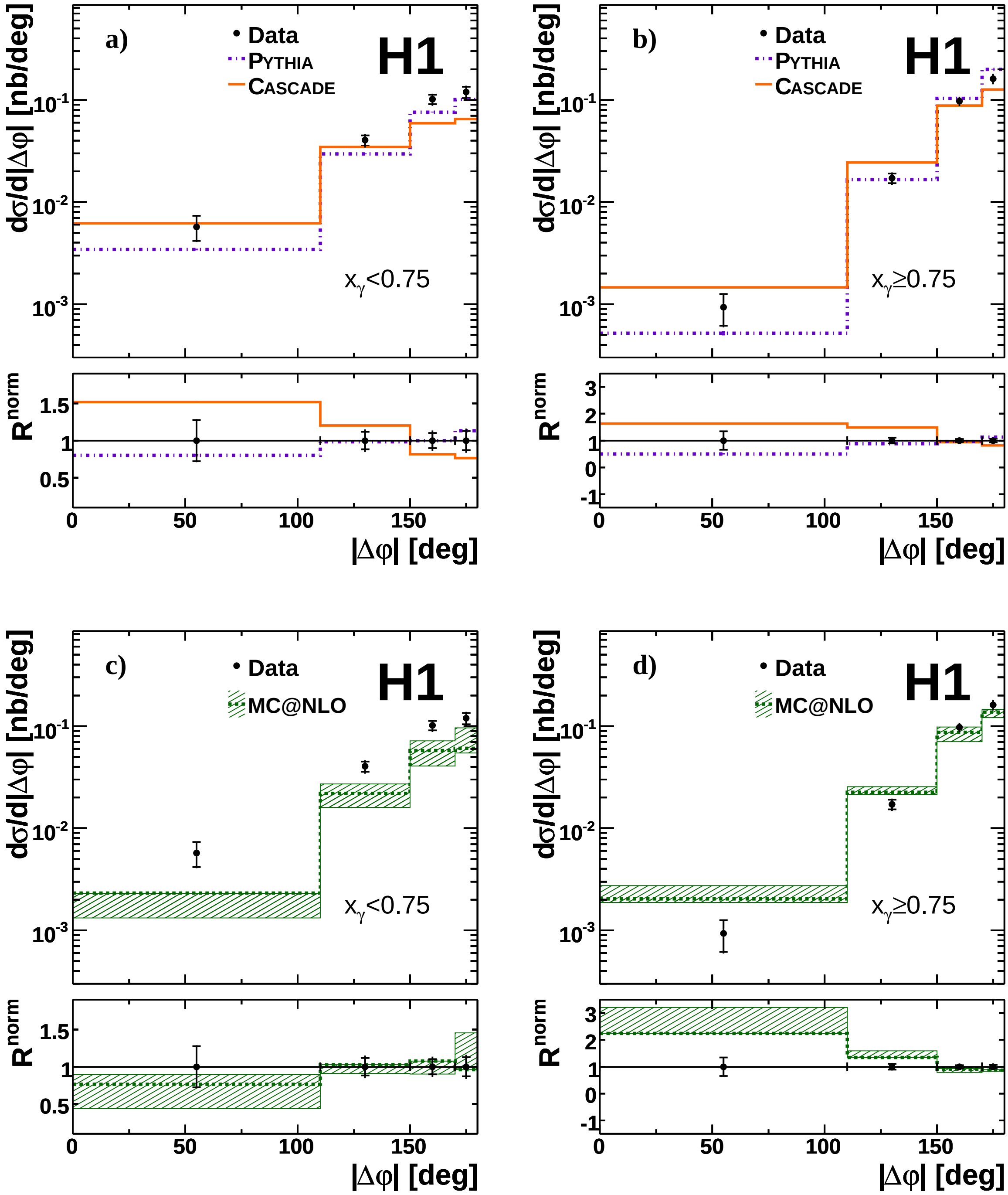

Figure 10: Single differential cross section for D^*-tagged dijet production as a function of the difference in azimuthal angle $\Delta\varphi$ in two regions of x_γ compared to predictions of PYTHIA, CASCADE and MC@NLO. The normalised ratio R^{norm} (see text) is also shown.